Cement and Concrete Research 170 (2023) 107198

Contents lists available at ScienceDirect

Cement and Concrete Research

journal homepage: www.elsevier.com/locate/cemconres

Understanding the gel compatibility and thermal behavior of alkali activated Class F fly ash/ladle slag: The underlying role of Ca availability

Y. Luo [a], H.J.H. Brouwers [a], Qingliang Yu [a,b,*]

[a] Department of the Built Environment, Eindhoven University of Technology, P.O. Box 513, 5600MB Eindhoven, the Netherlands
[b] School of Civil Engineering, Wuhan University, 430072 Wuhan, PR China

ARTICLE INFO

Keywords:
Geopolymer
Ladle slag
Ca availability
Elevated temperature

ABSTRACT

The gel compatibility in calcium contained geopolymers remains a controversial topic. This work aims to clarify the role of Ca availability in determining the geopolymerization of alkali-activated ladle slag/Class F fly ash blends. The results show that the product layer wrapping around slag particles largely governs the Ca diffusion into the environment, enabling the development of two separated gels, namely C-(N)-A-(*S*)-H and N-(C)-A-S-H type gel. A dense matrix consisting of geopolymer gel and Ca-enriched gel is achieved with 8 % of Na_2O while increasing Ms. intensifies the incompatibility between two gels, leading to microcrack formation and lowered mechanical strength. The competition between different reaction mechanisms of the two gels predominates the initial properties and thermal performance of the hybrid binder. A thermal degradation model of hybrid geopolymer co-existing geopolymeric gel and Ca-enriched gel is proposed to describe the influence of gel compatibility on the thermal behavior of Ca incorporated geopolymer.

1. Introduction

Geopolymer binder has attracted keen scientific interest as an environmentally-friendly alternative to Ordinary Portland cement (OPC) [1–3]. Resulting from alkaline activating industrial wastes, such as fly ash (FA), incineration bottom ash, and slag, this binder material enables a significantly low CO_2 emission [1,4,5]. With its typical three-dimensional aluminosilicate framework, geopolymers offer several advantages, for instance, low autogenous shrinkage, high temperature and acid resistance, and high immobilization capacity of toxic metals [2,6–8]. However, some major concerns for sole FA-based geopolymer such as relatively low early age mechanical strength and energy-consuming curing process stimulate growing interest in calcium-incorporated hybrid geopolymer binder. The incorporation of calcium sources such as OPC and ground granulated blast furnace slag (GGBFS) into aluminosilicates can alter the gel composition with promoted characteristics [5–7]. In this case, the phase assemblage becomes complicated in a blended Na_2O-CaO-Al_2O_3-SiO_2 system. Various studies regarding the Ca content in the blended geopolymer system have been performed, but the gel composition is still under disputation, including N-A-S-H, N-(C)-A-S-H, C-A-S-H, C-(A)-S-H as Ca concentration varies [9–12]. Furthermore, the binder gel compatibility in calcium incorporated geopolymer system is seen as another controversial topic, regarding whether the system develops two separated gel phases as C-A-S-H and N-A-S-H or an interacted N-C-A-S-H gel phase [10,11,13–15]. The compatibility study is of great importance, because the way hybrid gels coexist, as well as the discrepant characteristics of two gels, such as different gel structures, reaction kinetics, and drying shrinkage, can pose an adverse effect on the long-term durability of blended systems [16].

In general, the incorporation of calcium in the geopolymer system further complicates the reaction process, since the content of calcium, its presence in glassy or crystalline, and its availability (release rate) have a significant influence in determining the reaction pathway and gel composition/structure. Yip et al. [10,15] compared the role of calcium in geopolymerization by applying calcium silicates in form of amorphous and crystalline as a co-precursor with FA or metakaolin. Their results suggested that the alkalinity and extent of Ca dissolved from varied calcium silicate sources impacts the relative amount of Al substituted C-S-H gel and geopolymeric gel, which further influences the gel composition and mechanical strength. García-Lodeiro et al. [16] directly added soluble Ca into geopolymer gel, and a N-A-S-H gel containing Ca with preserved 3D structure was obtained. This reported phenomenon is discrepant from other works that observed the formation of chain-like C-(A)-S-H phases with the addition of initially activated Ca

* Corresponding author at: Department of the Built Environment, Eindhoven University of Technology, P.O. Box 513, 5600MB Eindhoven, the Netherlands.
E-mail address: q.yu@bwk.tue.nl (Q. Yu).

https://doi.org/10.1016/j.cemconres.2023.107198
Received 16 December 2022; Received in revised form 20 April 2023; Accepted 3 May 2023

sources and aluminosilicates [9]. The studies discussed above revealed that the Ca release rate/degree relative to geopolymerization reaction also plays a vital role in determining the binder gel composition, which may help to understand the gel compatibility in a hybrid geopolymer system. However, scarce attempts have been devoted to disclosing the reaction mechanism of Ca involved geopolymer system from the viewpoint of Ca availability. There is still a lack of understanding on the impact of Ca availability on the reaction mechanism and gel composition of hybrid geopolymers.

On the other hand, it has been revealed that Ca has a profound influence on the thermal behavior of the geopolymer system. Recent studies have been extensively carried out on the thermal resistance of hybrid geopolymers containing calcium sources (i.e., slag, calcium hydroxide, etc.) and aluminosilicate source (i.e., fly ash, metakaolin) [13,17–20]. The major conclusion is that the incorporation of Ca degrades the structural integrity and mechanical properties under high temperatures due to the interruption of geopolymerization and formation of C-(A)-S-H phases that are prone to dehydration/decomposition under high temperatures. Here, given the controversial and complex phase assemblage of hybrid geopolymers, very rare studies take gel compatibility into consideration to explore the thermal degradation mechanism of hybrid geopolymers. As known, N-A-S-H and C-A-S-H gel exhibit distinct thermal behavior under high temperatures. In this case, the relative content of each phase, how they bond together, and their interaction would have a significant influence on the thermal performance of the blended system. But a thorough understanding of the possible influence of gel compatibility on the thermal performance of Ca incorporated geopolymer system is not yet available.

Ladle slag (LS) is a by-product of the steel manufacturing process. Because of the particular secondary refinery process and the applied cooling technique, LS shows a high crystallinity, with calcium aluminates (CAs), namely mayenite ($C_{12}A_7$), and tricalcium aluminate (C_3A) as the main mineral phases [21]. Up till now, nearly 80 % of LS production is deposited in landfills and its valorization remains extremely low [22]. Despite the fact that CAs, especially $C_{12}A_7$, are known to be highly hydraulic and can react quickly with water, their content and reaction rate in LS varies between steel plants and production processes, resulting in varied reactivity with water [23,24]. To improve LS reaction efficiency and degree, there is a growing interest in alkali activation on LS, which turns out to be a promising pathway for reutilizing LS as a source of calcium and aluminium. The dissolution, as well as the reaction of crystalline calcium aluminates, is closely dependent on the alkaline content and SiO_2/Na_2O ratio [25–27]. This provides the possibility to utilize LS as a controllable calcium source by tailoring alkaline activator composition. In our previous study [28], with a moderate alkali environment, LS shows a positive effect on the geopolymer system attributed to its unique reaction process. Nevertheless, the fundamental mechanism of the dissolution and reaction of LS under alkaline activation is still not clear.

In light of the above knowledge gaps, this study aims to clarify the role of Ca availability in determining the gel composition of alkali-activated FA/LS (AAFL) and reveal the underlying mechanism. LS is used as a Ca source, and the alkali activator with tailored Na_2O percentage and silica modulus is applied as a tool to control its dissolution and reaction. The physicochemical properties of the obtained hybrid geopolymer are investigated by monitoring the workability, reaction products assemblage and compatibility, microstructure, and mechanical strength. High temperature exposure tests are carried out to investigate the influences of gel compatibility on the thermal behavior of hybrid binders. The results provide new insights into the gel compatibility of blended geopolymer systems and reveal the underlying reaction mechanism of the AAFL system. Additionally, a thermal degradation model of geopolymeric gel and Ca-enriched gel co-existing binder is proposed.

2. Experimental design

2.1. Materials

In this work, the investigated blended precursor consists of ladle furnace slag (LS, provided by Tata Steel, the Netherlands) and class F fly ash (FA, purchased from Vliegasunie, The Netherlands). The received FA was directly used and LS was collected from stockpiles in Tata Steel, following the pre-treatment described in Section 2.3.1. As shown in Fig. 1, a similar particle size distribution was achieved with the average particle size (d_{50}) of 13.99 μm and 13.96 μm for FA and LS respectively, determined by the laser particle size analyzer (Mastersizer 2000, UK). As observed by the scanning electron microscope (SEM) in Fig. 2, FA and LS have different shapes. As presented in Table 1, the chemical composition of LS and FA were determined by X-ray fluorescence (XRF, PANalytical Epsilon 3), the specific density was measured via the helium pycnometer (AccuPyc II 1340, Micromeritics), and the specific surface area was determined by the laser particle size analyzer. The crystalline phase assemblage was characterized by X-ray diffractometry (XRD, Bruker D4 PHASER), as shown in Fig. 3. FA exhibits a hump between 15 and 35° owing to the presence of amorphous phases, with traces of quartz (SiO_2), mullite ($Al_{1.69}Si_{1.22}O_{4.85}$), hematite ($Fe_2O_3$), magnetite ($Fe_3O_4$). LS shows a high crystallinity. Hydrated phases such as Hydrogarnet (C_3AH_6) and Hydrotalcite ($Mg_{0.667}Al_{0.333}$) $(OH)_2(CO_3)_{0.167}(H_2O)_{0.5}$ are detected due to the weathering of slag when disposing in stockpiles. Apart from that, calcium aluminates including Mayenite ($C_{12}A_7$), and Tricalcium aluminate (C_3A) are observed as major phases, indicating the presence of reactive phases even after weathering. To determine the weathering degree of the applied LS, thermogravimetry/differential scanning calorimetry (TG/DSC) analysis was carried out, and the result is compared with FA in Fig. 4. A total mass loss of 10.81 wt% is observed until 1000 °C. The main weight loss peak at around 300 °C is attributed to C_3AH_6 [29], and slight mass losses at around 150 and 450 °C are associated with metastable calcium aluminate hydrates (CAH_{10}, C_2AH_8) [29,30] and portlandite, respectively. Notably, owing to the complexity of LS disposal, for instance, the season, weather, stacking age, etc., it is very challenging to control the slag weathering degree. According to the variability among raw LS (See Appendix Fig. A1), the reactivity of raw LS may vary due to different weathering degrees, nevertheless, the mineralogy compositions of LS from different batches are identical as the slag production follows the same protocol. Thus, the applied LS demonstrates sufficient robustness for further investigation.

As for the alkali activator, the analytical level of sodium hydroxide pellets (99 wt%) and sodium silicate solution (27.69 wt% SiO_2, 8.39 wt

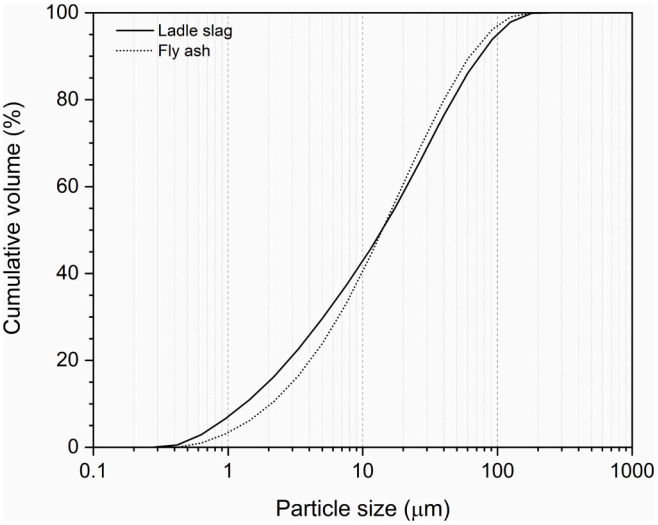

Fig. 1. Particle size distribution of raw materials.

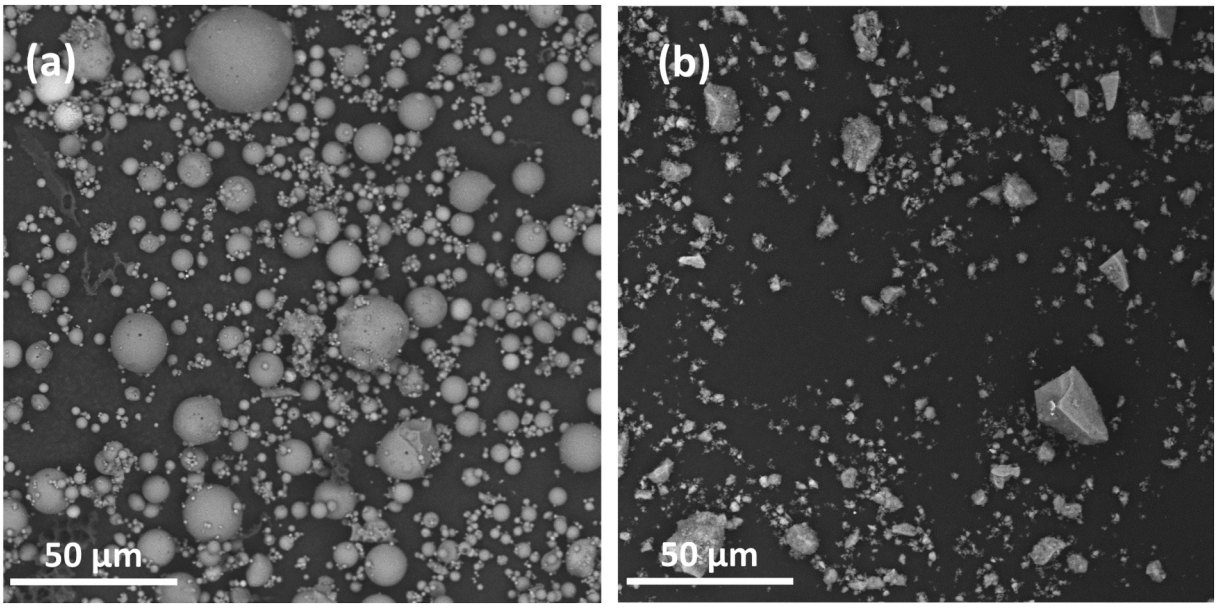

Fig. 2. SEM images of (a) FA and (b) LS powder.

Table 1
The chemical composition (wt%) and loss on ignition of Class F fly ash and ladle slag.

Oxides	Fly ash	Ladle slag
SiO_2	54.57	2.32
Al_2O_3	21.60	23.19
CaO	6.12	55.11
Fe_2O_3	9.04	4.44
MgO	1.17	2.21
SO_3	0.41	0.61
K_2O	2.85	–
Others	2.13	1.31
LOI (1000 °C)	2.11	10.81
Specific density (g/cm^3)	2.14	2.65
Specific surface area (m^2/g)	1.10	1.53

% Na_2O, 63.9 wt% H_2O) were applied. Distilled water was used to control the water to binder ratio.

2.2. Mix design and sample preparation

In terms of mix design, two levels of equivalent sodium percentage (6 wt% and 8 wt%, denoted by N6, N8) were applied to tailor the alkaline environment, and three Si moduli (Ms = 1.0, 1.4, 1.8, denoted by S1.0, S1.4, S1.8) were investigated at each alkali level. The activator composition is listed in Table 2. The desired activators were synthesized by mixing a specific amount of NaOH, water glass, and distilled water, thereafter, cooled for 24 h to room temperature before utilization. According to our previous work [28], the LS addition has a significant influence on the workability, and a high LS substitution always results in poor workability, hence the blend mass ratio of LS to FA was set as a constant of 20/80 and the mass ratio of water to binder was 0.35 in all samples. The mix proportion is shown in Table 3.

A 5 L Hobart mixer was applied for making the paste specimens. Firstly, dry precursors were mixed until a homogeneous state was reached, followed by the addition of a certain amount of activator while slowly stirring. The slurry was stirred at a low speed for 30 s and at a high speed for another 30 s. Subsequently, the mixture was cast into plastic molds (40 × 40 × 160 mm^3) and vibrated for 1 min. The paste specimens were firstly cured at ambient temperature (20 °C) in the sealed molds for 24 h before another 24 h of 60 °C curing. Afterward, the hardened specimens were demolded and cured at ambient temperature under a sealed condition until a certain age of characterization.

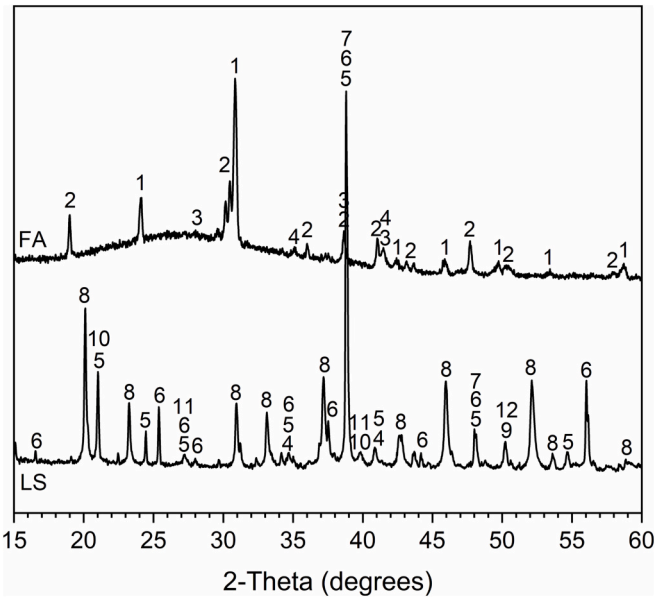

Fig. 3. XRD patterns of raw materials.
1-Quartz, 2-Mullite, 3-Hematite, 4-Magnetite, 5-Mayenite, 6-Tricalcium aluminate, 7-Dicalcium silicate (C_2S), 8-Hydrogarnet, 9-Periclase, 10-Portlandite, 11-Hydrotalcite, 12-Iron.

2.3. Methodology

2.3.1. Raw material treatment and characterization

After being collected from stockpiles, the weathered LS was dried in the oven at 105 °C for 24 h to remove free water. Then, by applying a disc mill (Retsch, RS 300), 600 g dried slag (material feed size <20 mm) was added into a 2000 mL grinding jar and milled for 5 min to obtain the desired particle sizes.

The particle size distribution and specific surface area were determined by a laser particle size analyzer (Mastersizer 2000, UK). The

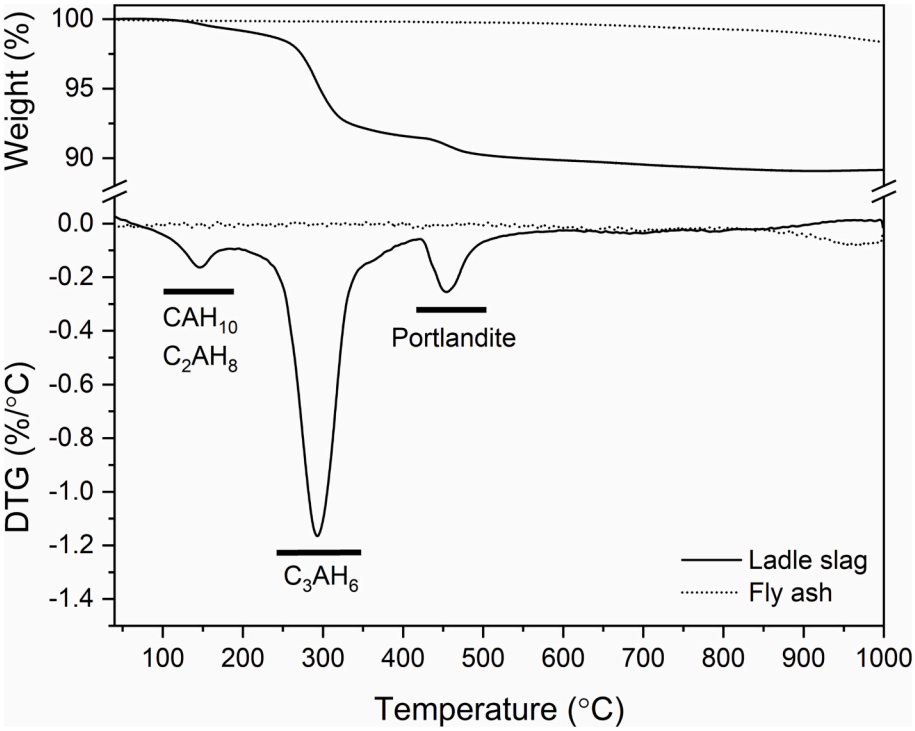

Fig. 4. TG-DTG analysis of raw materials.

Table 2
Chemical composition of working solutions.

Activator	Na_2O (wt%)	SiO_2/Na_2O modulus (Ms, mol.%)	Oxide composition (wt%)			pH
			Na_2O	SiO_2	H_2O	
N6S1.0	6	1	12.5 %	12.1 %	75.4 %	13.6
N6S1.4	6	1.4	12.0 %	16.2 %	71.8 %	13.6
N6S1.8	6	1.8	11.5 %	20.0 %	68.5 %	13.6
N8S1.0	8	1	15.3 %	14.8 %	69.9 %	13.5
N8S1.4	8	1.4	14.5 %	19.7 %	65.9 %	13.6
N8S1.8	8	1.8	13.8 %	24.0 %	62.2 %	13.5

Table 3
Mix proportion of investigated samples.

Sample code	Ladle slag	Fly ash	NaOH	Waterglass	Water	w/c[a]
N6S1.0	200	800	54.7	210.0	215.8	0.35
N6S1.4	200	800	45.6	294.0	162.2	0.35
N6S1.8	200	800	36.5	378.0	108.5	0.35
N8S1.0	200	800	72.9	280.0	171.1	0.35
N8S1.4	200	800	60.8	392.0	99.5	0.35
N8S1.8	200	800	48.7	503.9	28.0	0.35

[a] The total water content consists of the added distilled water and the water in water glass solution.

sample was added into the dispersant (2-propanol), dispersed by high-speed mechanical mixing coupled with ultrasound for 1 min to de-agglomerate the particles and eliminate air bubbles before characterization.

The specific density was measured on the powdered/crushed sample via the helium pycnometer (AccuPyc II 1340, Micromeritics).

2.3.2. Workability

The flowability of the slurry was determined by the flow table test following EN 1015–3 [31]. The paste was poured into a Hägermann cone (base diameter: 100 mm, top diameter: 70 mm, height: 50 mm) and allowed to spread freely in a flow table. After 5 min spreading, two diameters were collected from perpendicular directions, and the average value was adopted for each mixture. The setting times of mixtures were determined according to EN 196–3:2016 [32] by applying a Vicat needle apparatus under an ambient environment (20 °C, 60 % of RH). The moment of adding the activator into the dry precursor was set as zero time. The time at which the needle sinks no >0.5 mm is collected as the final setting time.

2.3.3. Reaction kinetics

The reaction kinetics of mixtures were investigated by using an isothermal calorimeter (TAM Air, Thermometric). For different mixtures, the content of dry precursors and activator were set proportionally following the mix composition shown in Table 3. About 9.5 g of pastes were mixed in the ampoule for 1 min to reach a homogenous state and then loaded into the calorimetry immediately. As the change of working temperature during the measurement would largely impact the precision of calorimetric measurements, a constant temperature of 20 °C was applied. For each mixture, the tests were conducted for 7 days and the results were normalized by the mass of the solids.

2.3.4. Microstructural characterization

The porosity was calculated according to

$$Porosity\% = \left(1 - \frac{\rho_b}{\rho_s}\right)\% \quad (1)$$

where ρ_s is the specific density and ρ_b represents the bulk density.

Among these, the bulk density was calculated by dividing the mass by the volume of the cubic sample, and the specific density was determined following the same procedure mentioned in Section 2.3.1.

Mercury intrusion porosimetry (MIP) analysis was performed to determine the pore structure by applying a mercury porosimeter (AutoPore IV 9500, Micromeritics). Before the test, ambient temperature samples at the age of 28 days were immersed in isopropanol for 72 h and dried at 40 °C for 24 h to cease hydration, while the thermally treated samples were used directly. Cubic pieces with grain sizes between 2 and 4 mm were cut and tested.

2.3.5. Phase assemblage and microstructure analysis

The tested samples were collected at 28 days of curing, and the hydration process was ceased following the same protocol mentioned in Section 2.3.4. Afterward, for TG/DSC, FT-IR, and XRD analysis, the dried samples were ground into powder using a ball mill for a short time (30 s) to avoid over-grinding that might cause the change of crystalline structure, followed by passing through an 80 μm sieve. The samples for SEM and Micro-CT analyses were kept in their original shape. The collected samples were then stored in sealed bags in a desiccator in avoiding water immersion or carbonation before analysis. While samples after high temperature exposure were ground/cut and tested directly.

A Jupiter STA 449 F1 Netzsch instrument was applied for Thermogravimetry/differential scanning calorimetry (TG/DSC) analysis. The powder sample was heated up to 1000 °C at a heating rate of 10 °C/min with nitrogen as the carrier gas.

The mineralogical patterns of paste samples were determined by conducting the X-ray diffraction (XRD) characterization with a Bruker D4 PHASER equipped with a LynxEye detector and Co X-ray tube (Co K α1 1.7901 Å and K α2 1.7929 Å). The step length was set as 0.6 s, and the increment was 0.02° with a scanning range from 15° to 60°. Rietveld method was further carried out for crystalline phase quantification. By using an XRD-mill, the ground paste powder was milled and mixed with 10 wt% of internal standard (Silicon) for 15 min before testing. The data was analyzed by TOPAS Academic software v 5.0. The XRD file numbers and ICSD codes for the applied crystal structures are provided in Table 4.

The Fourier transform infrared spectroscopy (FT-IR) measurement was performed on powder samples by applying a Varian 3100 instrument equipped with attenuated Total Reflectance (ATR) accessories. An air background spectrum was applied beforehand for calibration. Then, the sample powder was placed onto the ATR crystal and pressed down using the swiveling press to ensure optimal contact between the sample and crystal. All samples were scanned 50 times and the wavenumber was arranged from 4000 to 400 cm^{-1} with a resolution of 1 cm^{-1}.

In order to determine the unreacted phases as well as reaction products, the PhAse Recognition and Characterization (PARC) software [33] was applied based on energy-dispersive spectroscopy (EDX) mapping. The tested samples were cut from the centre of the pastes at the age of 28 days. After stopping the hydration, the dried samples were impregnated with epoxy resin and polished to obtain a smooth and flat surface. Then the polished samples were coated with Pt by using a Quorum 150TS plus sputter coater with a current of 40 mA. The spectral image with EDX data was obtained via a JEOL (JSM-7001F) equipped with two 30 mm^2 SDD detectors. An accelerating voltage of 15 kV with a beam current of 6.2 nA was applied, and the step size (resolution) was 1 μm, with the region comprising of 512 × 384 pixels. The obtained EDX mapping data were further processed with PARC software according to the chemical composition of each point, and grouped into phases. An erosion filter was used to exclude the data from the phase boundaries for obtaining representative chemical compositions. Afterwards, pixels surrounded by no <8 pixels with the same chemical composition were adopted for analysis.

To selectively characterize the phase composition of hydration products, a Phenom Pro (The Netherlands) equipped with EDX was used. The same SEM samples were tested as mentioned above. The measurements were conducted in a Backscattered electron (BSE) mode under an accelerating voltage of 15 kV with 4000× magnification, with a working distance between 8 and 10 mm. The EDX measurements were carried out on the outer surfaces of the samples with the region comprising of 512 × 512 pixels. At least 60 points out of 10 regions are taken from each sample, in which points are carefully selected within the binder region and kept a sufficient distance away from unreacted precursors, following [11,34].

Micro-CT 100 (Scanco Medical AG, Switzerland) was applied for microtomography. The X-rays energy was set as 70 kV, 200 mA, and an aluminium filter of 0.5 mm was applied. The prismatic specimens (1 × 1 × 4 cm^3) were collected from the core part of the samples and tested with a pixel resolution of 6.6 μm. 634 image slices from a 4.18 mm thickness of sample were obtained with a picture resolution of 2048 × 2048, and the data were then gathered to reconstruct and visualize a 3D internal structure. Three sections of each sample were measured for representative results. Materials with varied densities exhibit different absorption tendencies under X-rays, therefore, the components can be identified and separated.

2.3.6. Mechanical property

The compressive strength test was conducted on halves of prismatic specimens at the age of 7 and 28 days following EN 196-1 [35]. The prism samples were halved by applying the three-point loading method without being subject to harmful stresses. Four replicates for each mixture were tested at the loading rate of 2400 N/s, and the average value was taken.

2.3.7. High-temperature properties

In order to compare the present results with previous studies on the thermal behavior of fly ash/slag based geopolymers, a similar thermal exposure procedure was selected according to [13,20,28,36–39], under the guarantee of providing structural integrity after elevated temperature exposure for further characterization. The tests were carried out on samples at the age of 28 days. Before the test, prismatic samples were pre-heated at 105 °C for 12 h to remove free water in order to prevent severe spalling or cracking according to previous literature [13]. The tested samples were then loaded into a muffle furnace and heated from room temperature to target temperature with a heating rate of 10 °C/min and kept at 800 °C for 1 h to reach the thermal equilibrium state. Afterward, the samples were naturally cooled down to room temperature inside the furnace and then sealed with plastic foil to avoid moisture immersion. For each mixture, three samples were tested under the same condition.

The thermally induced linear shrinkage of samples was determined by comparing the length of the prismatic samples before and after high temperature exposure. Three samples were measured for each mixture, and the average data were taken.

The mechanical strength test was carried out on cooled halves of the prismatic samples after high temperature exposure, following the same protocol as mentioned in Section 2.3.5. The average value of six replicate measurements was adopted as the residual strength value.

Table 4
Structural data of the phases used for XRD analysis.

Phase	#PDF-reference	ICSD
Quartz (SiO_2)	01-083-0539	83849
Mullite ($Al_{1.69}Si_{1.22}O_{4.85}$)	01-089-2813	43297
Magnetite (Fe_3O_4)	01-089-0951	31156
Hematite (Fe_2O_3)	01-089-2810	22505
Metallic iron (Fe)	01-085-1410	11146
Tricalcium aluminate (C_3A)	00-038-1429	1841
Mayenite ($C_{12}A_7$)	00-048-1882	62040
Dicalcium silicate (C_2S)	00-036-0642	81097
Gibbsite ($Al(OH)_3$)	00-007-0324	34393
Hydrogarnet (C_3AH_6)	00-024-0217	9272
Hydrotalcite ($Mg_{0.667}Al_{0.333}$) $(OH)_2(CO_3)_{0.167}(H_2O)_{0.5}$	01-089-0460	81963
Periclase (MgO)	01-071-1176	64928
Calcite ($CaCO_3$)	01-077-2376	40544
Portlandite ($Ca(OH)_2$)	01-087-0673	15471
Ca-Faujasite (Ca40Al80Si112O384 (H2O)116)	01-071-0936	176465
Nepheline ((Na, K)$AlSiO_4$)	01-085-1487	–
Wollastonite ($CaSiO_3$)	01-076-0186	–
Akermanite-Gehlenite (Ca_2(Mg0.5Al0.5 (Si1.5Al0.5O7))	01-079-2423	–

3. Results

3.1. Workability and reaction kinetics

It has been previously reported that geopolymer with the addition of LS always suffers from low flowability and fast setting problems [21]. As shown in Fig. 5a, a higher Na_2O of 8 % increases the flowability. Moreover, with a 6 % Na_2O, the flowability increases with a higher Ms. while an insignificant reduction of flowability with increasing Ms. is observed in 8 % of Na_2O sample. The workability of the mixture is mainly determined by the early age dissolution and polycondensation of raw materials, which is synergistically influenced by the nature of the precursor (fineness, composition) and activator (type, concentration, modulus) [40]. Here, the dissolution of precursors conducts at a relatively slow pace with a low Na_2O%. The higher Ms. increases the thickening of the activator which promotes the dispersion of the precursor particles as an effect of lubrication [41,42]. Thus, a higher flowability is resulted with the increased Ms. at 6 % of Na_2O. While at a higher Na_2O level, more environmental OH^- accelerates the dissolution process, and further increases flowability. The slight variation of flowability with increased Ms. is expected to be the co-effect of dispersion and dissolution. The setting time of samples is depicted in Fig. 5b. As compared to the setting of sole FA based geopolymer (>24 h at room temperature) [43], LS plays a dominant role in the observed setting behavior. This is because the C_3A and $C_{12}A_7$ react very quickly with water that easily causes flash setting. At a low Na_2O%, due to the limited content as well as weathering process of LS, the flash setting is avoided but still, the setting of hybrid geopolymer is largely shortened to <1 h. With increasing Ms., abundant soluble Si could attract more environmental ions that accelerate the formation of hydration products. While a higher Na_2O% is noticed to prolong the setting time, and the setting is further increased with rising Ms. The reason for this observation is not entirely clear, but it is possibly related to the dissolution kinetics that a higher alkalinity slows down the Ca dissolution rate according to solubility constant principle [44].

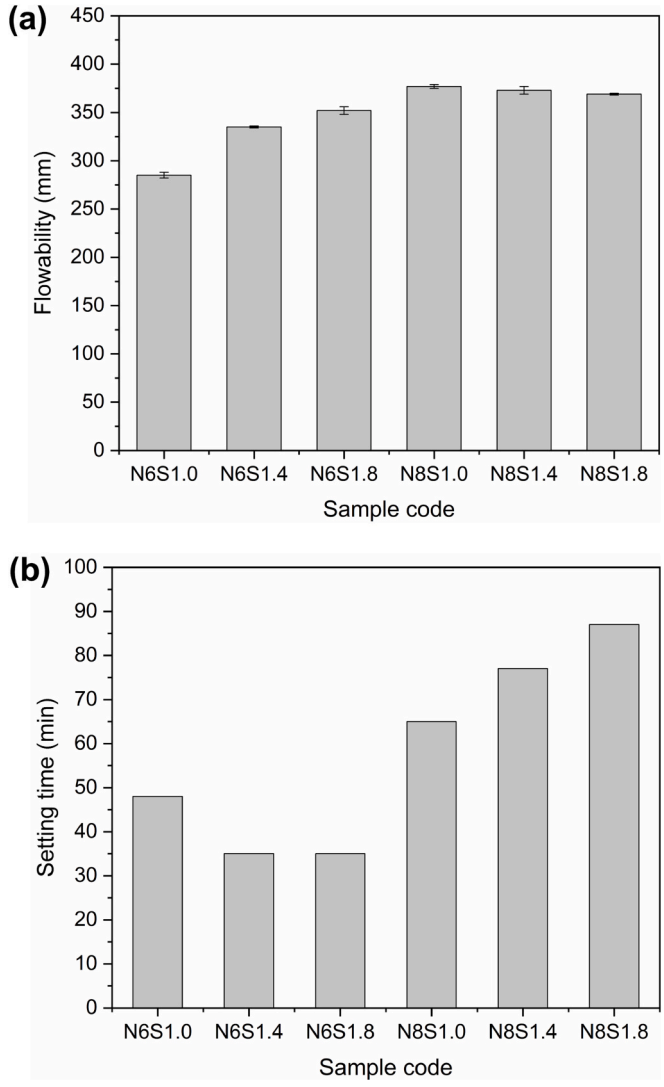

Fig. 5. Flowability and setting time of pastes prepared with different Na_2O% and activator modulus.

The observed phenomenon clarifies that the alkali activator parameters have a significant influence on the workability of the LS/FA binder. With the 20 % substitution of LS, the setting time is significantly shortened to a range between 35 and 87 min by tailoring Na_2O% and Ms., indicating the setting of FA-based geopolymer can be controlled/accelerated by introducing LS with a tailored activator.

The fresh property is further revealed by the reaction kinetics from isothermal calorimetry shown in Fig. 6. It should be mentioned that, as compared to the realistic curing process, the exclusion of 24 h 60 °C curing in the calorimetric test might result in relatively lower reaction heats than the actual value. But the results can still be used as a general index reflecting and comparing the trend of reaction rate among different mixtures. Fig. 6a depicts the heat evolution of mixtures for the initial 7 days. It should be mentioned that a single exothermic peak is detected during the measuring period for all mixtures. Such a sole peak phenomenon has been previously reported in FA geopolymer as well as LS/FA hybrid geopolymer [45,46], which is related to the dissolution of precursor, the initial formation of silicate and aluminate species, and their complexation with the sodium and calcium ions [47]. At a low Na_2O% of 6, an increasing heat flow intensity combined with a larger cumulative heat release is observed with raising Ms., indicating its contribution to the dissolution of solid raw materials as well as the early reactivity. This is in agreement with the shortened setting time and better flowability presented in Fig. 5. Accordingly, a higher Na_2O% largely promotes the reaction degree, with the highest heat flow peak intensity and largest cumulative heat release achieved with Ms. of 1.0.

3.2. Reaction products

The thermogravimetric (TG) and differential thermogravimetry (DTG) curves of samples are presented in Fig. 7. The samples with a high Na_2O% of 8 % exhibit a larger weight loss after 1000 °C. As shown in Fig. 7b, the main mass loss peak in the range of 100–300 °C is associated with the loss of bound water from the main hydration products, namely, N-A-S-H and C-A-(*S*)-H gel [48]. The second peak is assigned to the dehydroxylation of $Al(OH)_3$ (AH_3, around 260 °C) [49] and hydrogarnet (C_3AH_6) [28]. Additionally, a broad weight loss in temperature ranging from 500 to 800 °C mainly arises from the presence of $CaCO_3$ in different crystallinity [50]. The poorly crystallized calcite and amorphous $CaCO_3$ decompose at 500–600 °C, while the well-crystallized $CaCO_3$ decomposes at a later stage around 700 °C [51].

In general, the peak intensity of the main reaction products and AH_3 vary significantly as a function of Na_2O% and Ms., meaning that the activator has a significant influence on the reaction of both FA and LS. It is noted that at a Na_2O% of 6 % with the increasing Ms., the main weight loss peak is not only intensified but also slightly shifted to a higher temperature from 126 to 131 °C. Here, the higher amount of readily available silicates in the environment contributes to a higher degree of reaction with more gel phase and tightly bound water [52], intensifying the main mass loss peak. Accordingly, in samples with 8 % of Na_2O, a larger mass loss with the peak temperature shifting to 135 °C is detected. Nevertheless, the difference in the main mass loss peak among samples with different Ms. is insignificant, and the highest main mass loss peak is achieved with the lowest Ms. of 1.0, which is in accordance with

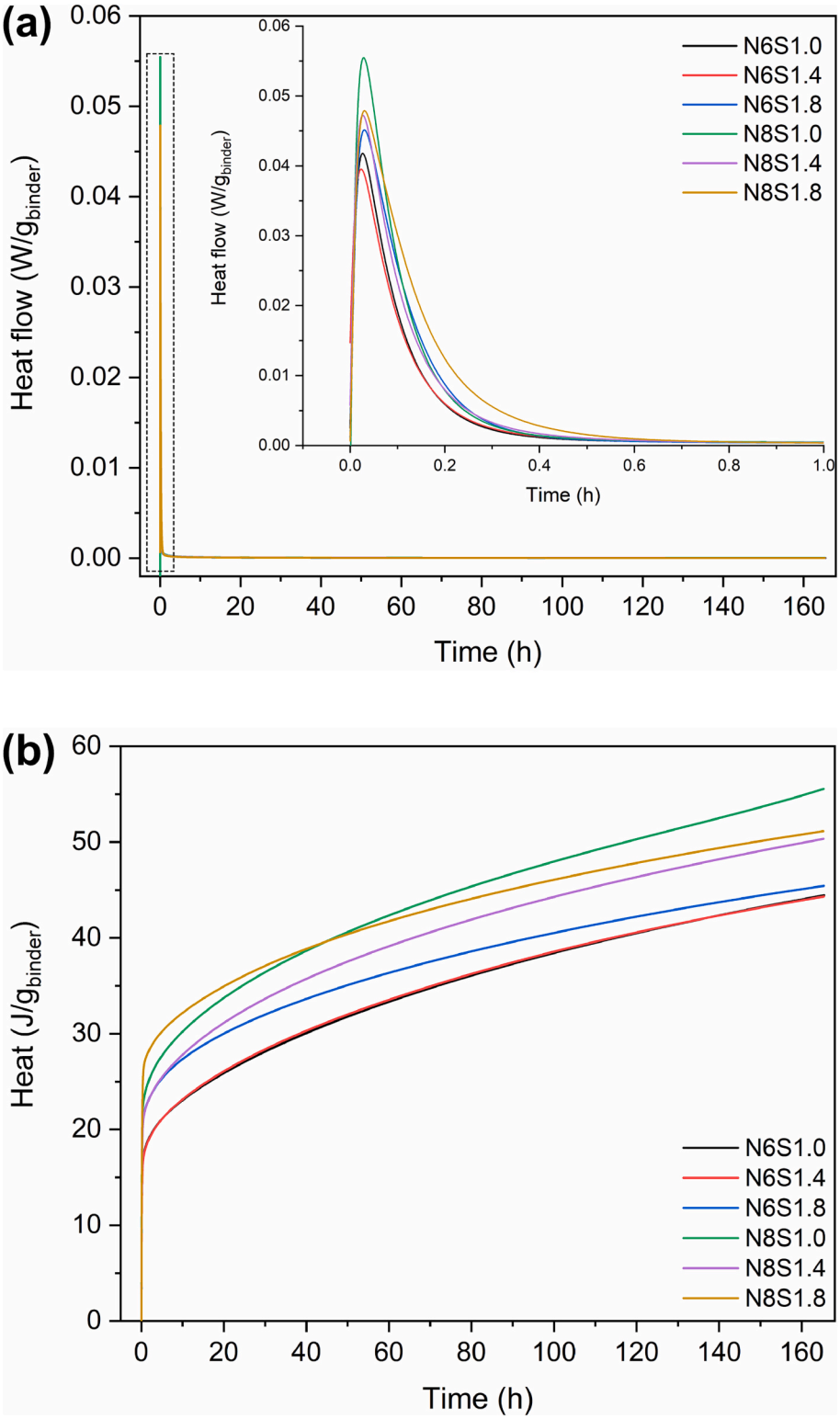

Fig. 6. Isothermal calorimetric response of samples, a) normalized heat flow, b) normalized cumulative heat.

reaction kinetics. As for AH_3, the corresponding mass loss peak is indetectable in samples with a lower Na_2O% due to its low content. While at a higher Na_2O%, the AH_3 peak is intensified as consistent with the previous discussion that a high alkali content promotes the dissolution of aluminosilicate species from the precursors. However, the AH_3 peak intensity is decreased with the increased Ms. It can be hypothesized that AH_3 tends to participate in the formation of aluminosilicate gels since more soluble silicates are introduced.

The infrared spectra of samples with different Na_2O% and Ms. are compared in Fig. 8a. The band in the range of 670–850 cm^{-1} is corresponding to the stretching vibrations of Si–O–Si, attributed to crystalline quartz introduced by FA. The typical adsorption band of the Si-O-T (where T represents Si or Al species) is observed at around 980 cm^{-1} in all samples, resulting from the phase overlapping from precursors and

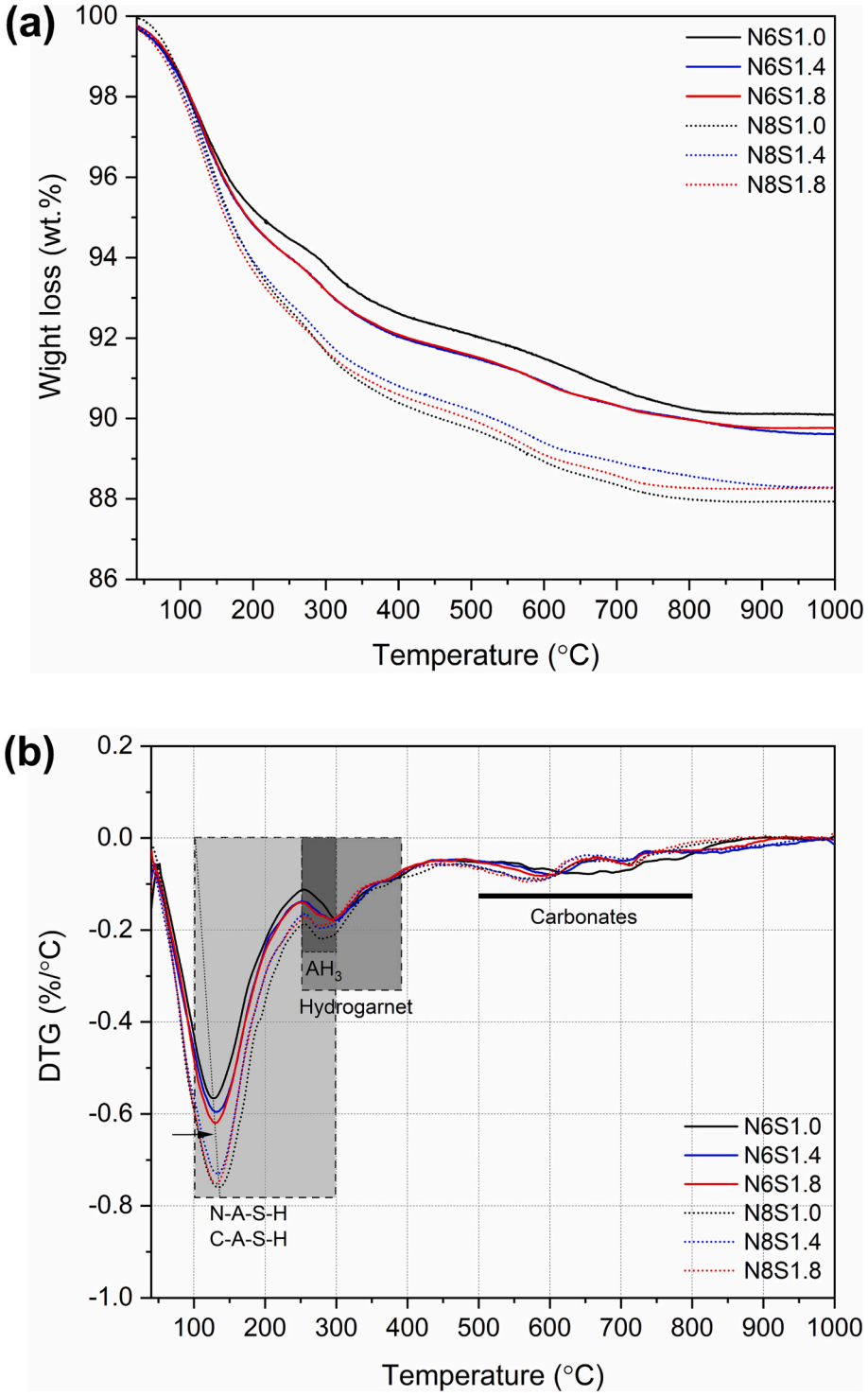

Fig. 7. Thermal analysis of pastes with different Na_2O% and Ms. at 28 days, (a) TG curves; (b) DTG curves.

aluminosilicate phases. The adsorption of 1643 cm^{-1} and 3418 cm^{-1} are identified as the bending vibrations of physically and chemically bound water and stretching vibrations of O—H bonds respectively. Series of spectra at 1463 cm^{-1} and 1404 cm^{-1} are both assigned to the different vibration modes of CO_3^{2-} [53], confirming the presence of carbonates, which is in line with the calcite detected in TG results. Additionally, the peak ascribed to periclase at 3750 cm^{-1} [54] is insignificant, indicating the relatively low presence of periclase.

It is known that the typical absorption band of the Si–O-T bridge bond reflects the polymerization process within a hybrid system. Here, its position change as a function of Na_2O% and Ms. is presented in Fig. 8b. At a lower Na_2O% of 6 %, the main band shifts to lower wavenumbers with the increased Ms. This is related to more readily available silicates in the environment that contributes to a higher polymerization degree with more silica-rich cross-linking [55]. While it is noticed that at a higher Na_2O%, the Si-O-T bond is decreased to a lower wavenumber. Because more $Al(OH)_4^-$ is released from precursors, and incorporated into gels as evidenced by TG results, consequently resulting in the shift of Si-O-T band to a lower position [56]. Nevertheless, the Si-O-T band shifts back to a higher wavenumber with a

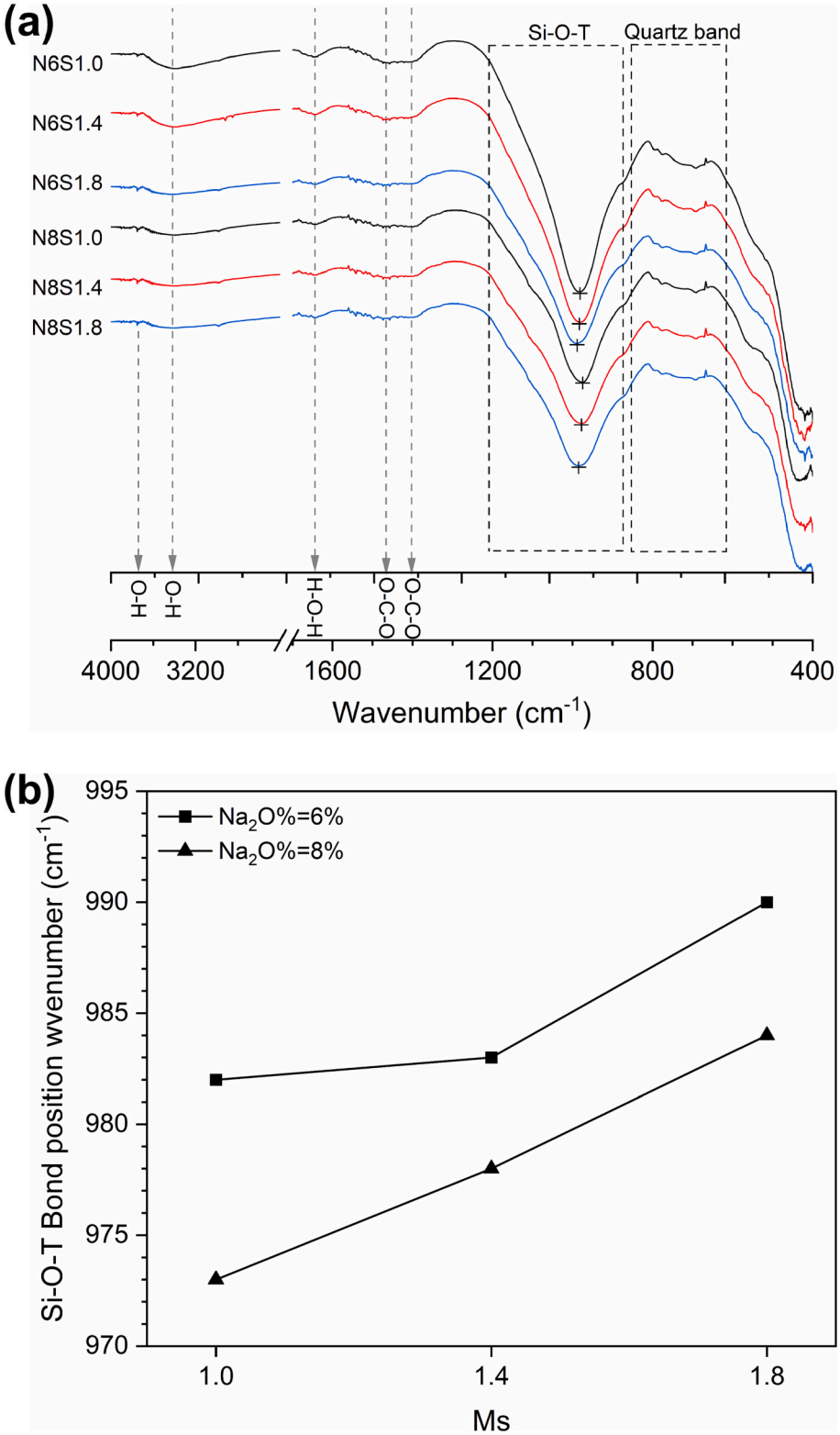

Fig. 8. a) FTIR spectra of pastes with different Na_2O% and Ms., b) Si-O-T bond wavenumber variation of samples as a function of Na_2O% and Ms.

higher Ms. This is because the Si species are directly available in the solution from the activator in case of a higher Ms., while the dissolution of $Al(OH)_4^-$ from precursors is slower as compared to $Si(OH)_4^-$, hence a higher level of silica cross-linking is promoted in geopolymeric gel. Another feature should be highlighted is that the shape of the Si-O-T bond transforms from a narrowed to a broad shape with a lower intensity since the Na_2O% and Ms. increase respectively. This variation should be associated with the formation of either hybrid N,C-A-S-H gel or separated C-A-S-H and N-A-S-H gel, because the variation of gel composition/structure or relative content between different aluminosilicate gels may alter the shape of the Si-O-T bond [57,58].

The crystalline phases of samples with different Na_2O% and Ms. are presented in Fig. 9. In general, there is no new crystalline phase observed in most samples except for N8S1.0. The typical phases such as

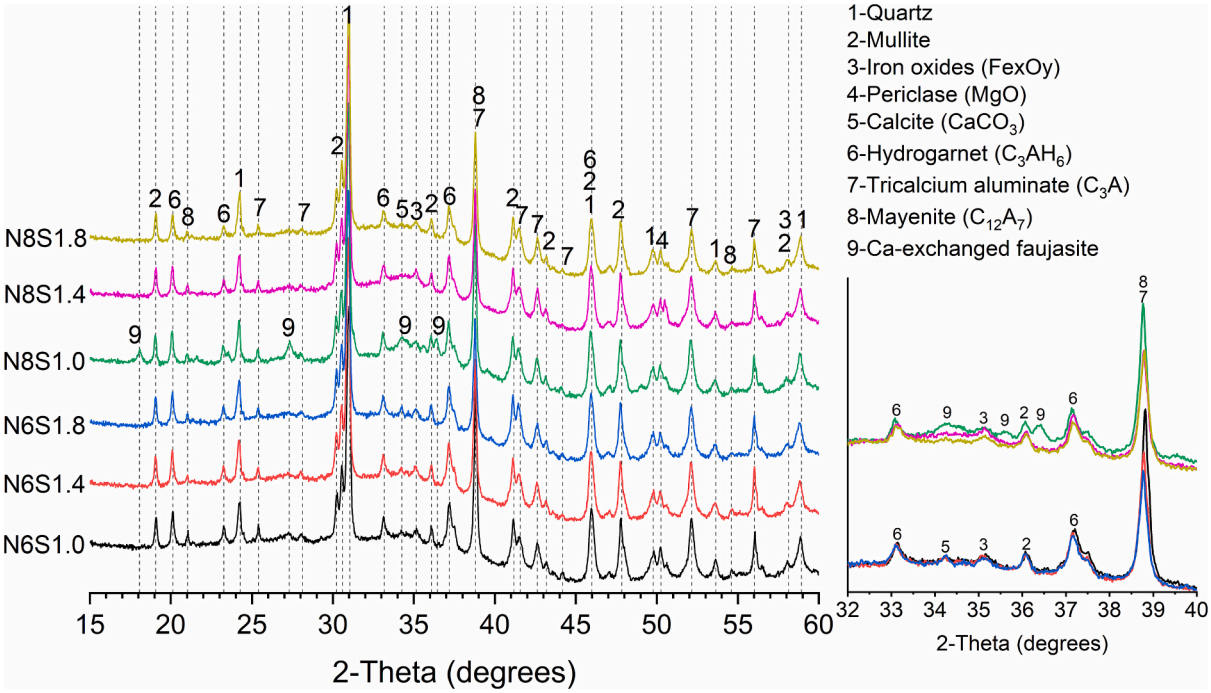

Fig. 9. XRD patterns of pastes at the age of 28 days.

quartz, mullite, iron oxides, periclase, calcite, and hydrogarnet are introduced by raw precursors as observed in Fig. 3. The remanent C_3A and $C_{12}A_7$ indicate the limited reaction degree of calcium aluminates. This is due to, despite the calcium aluminates can react with water very fast, the hydration product is a continuous plate-shape, which gradually covers the unhydrated particles and hinders additional hydration [59].

To further determine quantitatively both the crystalline and amorphous phases variation as a change of alkali percentage and Ms., the Rietveld analysis is carried out as summarized in Table 5. The results reveal that crystalline phases from FA such as quartz, mullite, hematite, and magnetite remain unchanged or slightly decreased, and the reactive phase in FA is mainly amorphous, which is undetectable via XRD. Thus, FA is not included in the comparison. Moreover, it is further proved that the activator can influence the dissolution of LS, in which the amount of C_3A, $C_{12}A_7$, and C_3AH_6 (hydrogarnet) are increasingly lessened with a higher Na_2O% and Ms., and the reduction of the calcium aluminates is more sensitive to Na. As discussed in previous works on both calcium aluminate cement [25] and LS [28], calcium aluminate phases and the hydrated C_3AH_6 under a highly alkaline environment with the presence of silicate can react into siliceous hydrogarnet and calcium aluminosilicate hydrate gel, which might be crystallized into zeolitic phases, following the routes:

$$CA \xrightarrow{OH^-} C_3AH_6 \tag{2}$$

$$C_3AH_6 \xrightarrow{Silicate} C_3AS_nH_m + \underset{(Amorphous\ and\ crystalline)}{Calcium\ aluminosilicate\ hydrate} \tag{3}$$

This is consistent with the present work. Given the conversion of the amorphous phase in FA to aluminosilicate gel should not impact the total amorphous content, the observed amorphous content variation is mainly ascribed to the dissolution of LS. Here, a larger content of calcium aluminates and hydrogarnet are consumed with increasing Na_2O% and Ms., giving rise to an increase in aluminosilicate gel as evidenced by the higher amorphous content from 77.9 % to 81.3 %. In addition, a 1.3

Table 5
The mineral compound of the mixtures in comparison to raw ladle slag in wt% as determined by XRD-Rietveld analysis.

Mineral compound	LS	Mixtures					
		N6S1.0	N6S1.4	N6S1.8	N8S1.0	N8S1.4	N8S1.8
Tricalcium aluminate (C_3A)	22.9 (4.6)	4.0	3.6	3.6	3.3	3.0	2.8
Mayenite ($C_{12}A_7$)	4.4 (0.9)	0.7	0.6	0.5	0.6	0.6	0.6
Hydrogarnet (C_3AH_6)	27.5 (5.5)	4.8	4.7	4.6	4.4	4.1	3.8
Dicalcium silicate (C_2S)	2.2 (0.4)	–	–	–	–	–	–
Nordstrandite ($Al(OH)_3$)	1.1 (0.2)	–	–	–	–	–	–
Hydrotalcite ($Mg_{0.667}Al_{0.333}$) $(OH)_2(CO_3)_{0.167}(H_2O)_{0.5}$	0.5 (0.1)	–	–	–	–	–	–
Periclase (MgO)	2.8 (0.6)	1.1	0.9	0.8	1.0	0.9	0.8
Portlandite ($Ca(OH)_2$)	1.3 (0.3)	–	–	–	–	–	–
Metallic iron (Fe)	0.4 (0.1)	–	–	–	–	–	–
Ca-Faujasite ($Ca_{40}Al_{80}Si_{112}O_{384}$ $(H_2O)_{116}$)	–	–	–	–	1.3	–	–
Quartz (SiO_2)	–	4.4	4.2	4.3	4.0	4.0	4.1
Mullite ($Al_{1.69}Si_{1.22}O_{4.85}$)	–	5.4	5.3	5.3	4.9	4.9	4.9
Hematite (Fe_2O_3)	–	0.4	0.4	0.5	0.4	0.4	0.4
Magnetite (Fe_3O_4)	–	0.7	0.8	0.8	0.8	0.8	0.7
Calcite ($CaCO_3$)	–	0.6	0.6	0.6	0.8	0.7	0.6
Amorphous	36.9 (7.4)	77.9	78.9	79.0	78.5	80.6	81.3

() Content of mineral phases introduced by 20 wt% addition of LS is calculated.

wt% of Ca exchanged Faujasite phase is detected in the high Na_2O% sample, which should be crystallized from (N, C)-A-S-H gel followed by Eq. (3). As Ms. keeps increasing, this phase tends to disappear. It can be concluded that the Na_2O% promotes the crystallization of calcium exchanged zeolite, while it is more favourable to form N,C-A-S-H gel when there is a low Ca/Si under the circumstance of low Na_2O%, or high Na_2O% with high Ms.

Nevertheless, despite the comprehensive characterizations carried out above, the compatibility between geopolymeric gel and Ca-enriched gel in FA/LS system is still not clear since it is difficult to precisely differentiate them from the TG, FT-IR, and XRD results.

3.3. Gel phase identification

Due to the metallic iron introduced by LS, it is impossible to utilize Nuclear Magnetic Resonance (NMR) to characterize the gel properties. As learned in XRD-Rietveld analysis, the reaction products are mostly amorphous and can be easily identified with SEM, which makes the EDX a reliable indicator for selective analysis of gel composition. As shown in Fig. 10, a representative AAFL sample is evaluated with the PhAse Recognition and Characterization (PARC) analysis (the calculated average chemical compositions of different phases are presented in Appendix Table. A1). In contrast to XRD-Rietveld analysis, PARC analysis is capable of identifying different phases in either crystalline or amorphous forms.

In Fig. 10, combining the SEM image and phase map generated by PARC software, the unreacted FA (denoted as point A) can be easily distinguished since it exhibits a spheric shape, as also proved by a mix of quartz and mullite in PARC analysis. Moreover, clusters of LS (denoted as point B) are preferably formed, which is evidenced by the mix of calcium aluminates, calcium aluminate hydrates, C_2S, and periclase. Note that it could lead to the lubrication problem that partially explains the poor workability when utilizing LS as a co-binder in geopolymers. In addition, it is interesting to notice that two types of gel are differentiated in both SEM and the phase map. A rough and porous binder phase is observed as geopolymeric gel (point C, denoted as N-(C)-A-S-H in light green in phase map), in which the small portion of calcium should be resulted from the uptake of sodium in geopolymeric gel by environmental calcium as discussed above. Apart from that, a smooth and dense binder phase formed around LS particles is ascribed to calcium enriched aluminosilicate gel (point D, denoted as C-(N)-A-S-H in dark green in phase map) with high calcium, aluminium, and silicon, but low Na content.

To further learn the binder gel composition in different samples, selective EDX analysis is conducted on gel phases and the results are plotted in CaO-SiO_2-Al_2O_3 ternary diagrams as shown in Fig. 11. Interestingly, the binder gel phase distribution patterns are significantly varied in samples with different Na_2O%. Here, for the sample with a Na_2O% of 6 % in Fig. 11 a, the majority reaction product is geopolymeric gel with low calcium (N-(C)-A-S-H). The points are distributed in a larger area in samples with lower Ms., in which minor calcium enriched gel is also obtained. With increasing Ms., the cluster region is largely narrowed from Al-rich N-A-S-H gel to Si-rich N-A-S-H gel, in agreement with the FT-IR results. In terms of high Na_2O% samples, as shown in Fig. 11 b, unlike the concentrated clusters in lower Na_2O% sample, two separated clustered regions vertically lying on the ternary diagram can be distinguished: i) a low calcium substituted geopolymer gel, ii) a C-(N)-A-S-H gel with low sodium content. The ion proportion of gels varies significantly as a function of Ms. with a clear trend. The change in geopolymer gel along with Ms. is similar to that of low Na_2O% samples. In the compositional cluster of C-(N)-A-S-H type gel, the calcium content is positively related to aluminium but negatively to silicon, inferring that the phase composition is closely related to the reaction of LS to form C-A—H, as well as its ability of incorporating Si to form C-A-S-H. With the increased Ms., the clustered region increasingly approaches the raw LS, which is in accordance well with the XRD results that a higher Ms. promotes the dissolution and hydration of calcium aluminates. Furthermore, the gel phase composition is largely enriched with a higher Ms. since the C-A-H absorbs silicon to C-A-S-H, thus showing an enlarged cluster region, in which the silicon proportion varies approximately from 0 to 0.5.

At last, it should be emphasized that a balance of ion proportion is reached between those two gels, namely lower Ca, Al, and higher Na, Si in geopolymer gel; but higher Ca, Al, and lower Na, Si in calcium

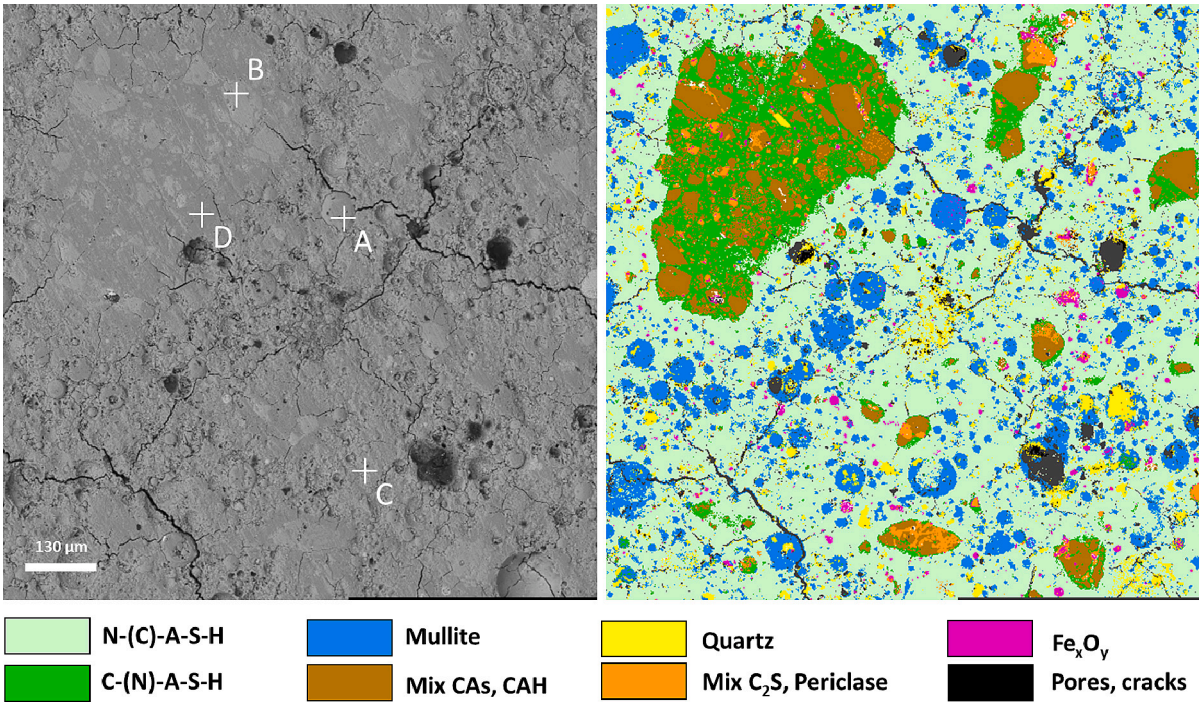

Fig. 10. SEM image of representative AAFL sample (left) and phase clustering generated with PARC software based on EDX (right).

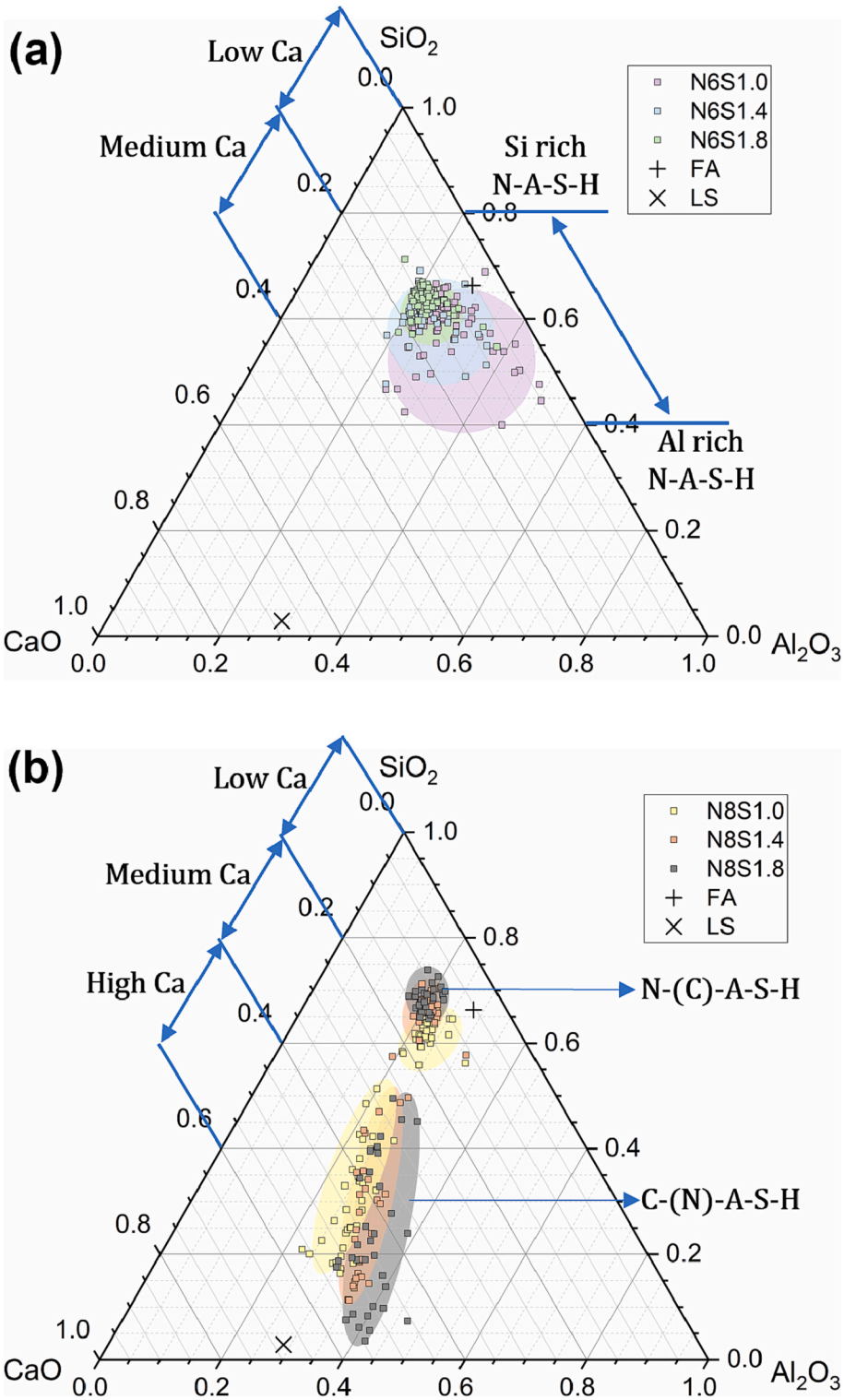

Fig. 11. Composition ternary diagram in CaO-SiO_2-Al_2O_3 of EDX analysis (normalized as 1) for the reaction products in samples at 28 days. Approximate regions of C-(N)-A-S-H determined from [14,60] and N-(C)-A-S-H determined from [11,16,61].

enriched gel with increasing Ms. This phenomenon indicates a continuous ion exchange process between the two gels with changing of Ms. and dissolving of raw precursors. As a result, a co-existence of two independent gels, namely N-(C)-A-S-H and C-(N)-A-S-H arising from FA and LS respectively, is obtained in the hybrid geopolymer system, especially for high Na_2O% samples.

3.4. Microstructure and mechanical properties

Fig. 12 depicts the microstructure of AAFL specimens with different Na_2O% and Ms. at the age of 28 days. Two distinct morphologies are identified in samples with different Na_2O%. With a low Na_2O%, the samples exhibit a loose structure with abundant unreacted precursor particles. This is mainly resulted from the relatively low reaction degree

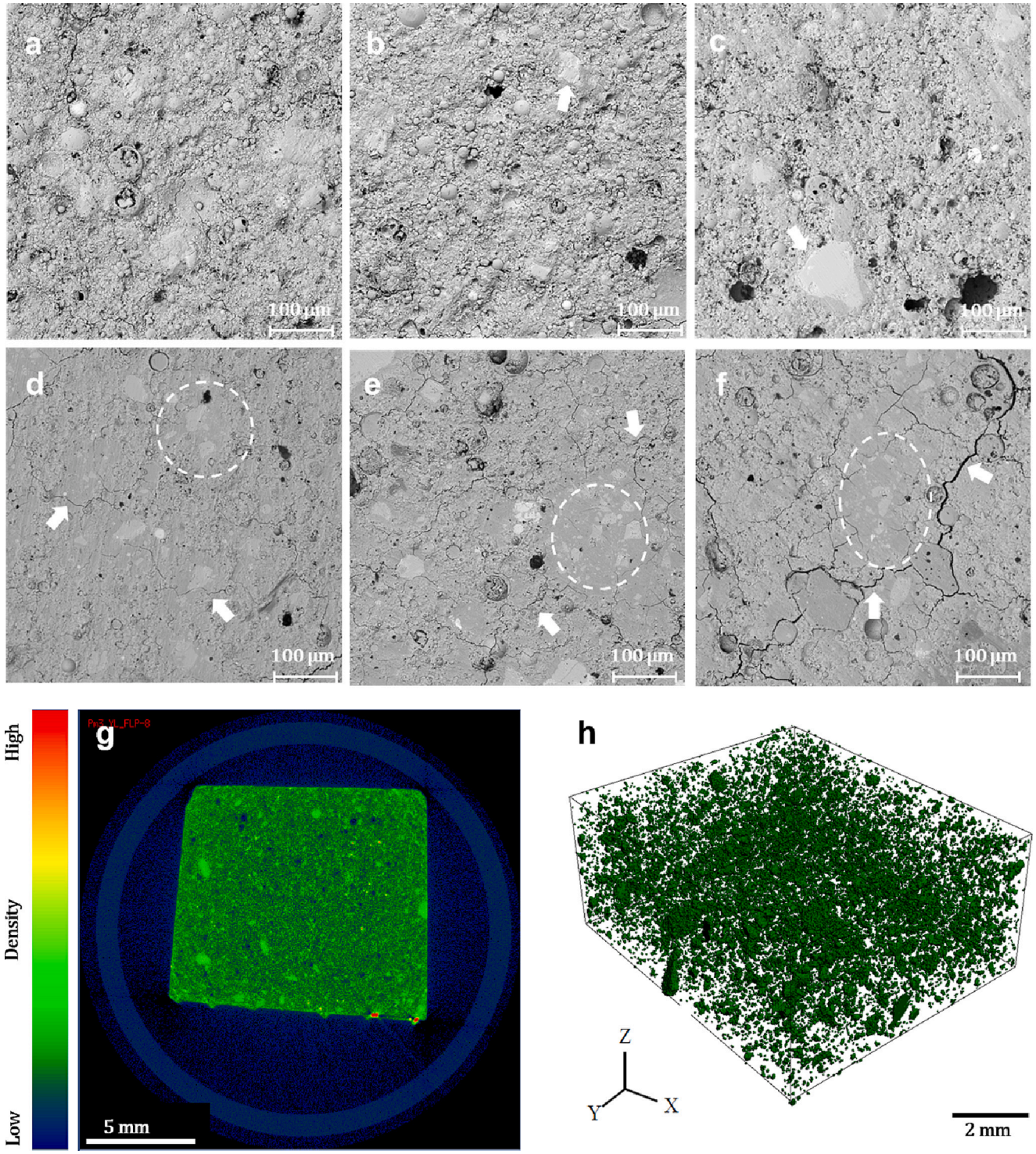

Fig. 12. SEM micrographs of AAFL specimens (a) N6S1.0, (b) N6S1.4, (c) N6S1.8, (d) N8S1.0, (e) N8S1.4, (f) N8S1.8; Micro-CT of N8S1.4 (g) 2D, (h) 3D image.

in the system with 6 % of Na_2O. Apart from that, increasing air voids are entrained, especially for sample N6S1.8, which should be resulted from the fast setting, as observed in Fig. 5. In contrast, a clearly denser structure with fewer remanent precursors is detected in samples with a higher Na_2O percentage. Here, the higher Na_2O% promotes the workability as well as the dissolution of the precursor, consequently resulting in a denser structure with more hydration products. The densely clustered phase formed around LS particles are observed in high Na sample but almost indetectable in low Na samples, which can be attributed to either the low reaction degree or the weak matrix that cannot protect the clustered structure during polishing. Moreover, visible microcracks originate along the boundary between the two different types of gels, which should be caused by gel incompatibility, for instance, the differences in autogenous shrinkage degree and gel formation kinetics [62,63]. Moreover, the microcracks are noticed to be increasingly visible in samples with higher Ms. It can be concluded that the increasing Ms. further intensifies the incompatibility between the two different gel phases, resulting in the formation of more microcracks.

To learn the distribution of LS based clusters in the matrix, Micro-CT scanning is carried out on sample N8S1.4. In Fig. 12g, the dense clusters

are differentiated from the loose geopolymeric binder and highlighted as light green in contrast to dark green geopolymer binder, the micro-tomography of plain FA geopolymer and LS/FA hybrid geopolymer are given in Appendix (Fig. A2). According to the reconstructed 3D structure, as shown in Fig. 12h, the LS based clusters (represented as green particles) are scattered in the whole matrix, which further proves the separate existence of LS based gel and geopolymeric gel. Moreover, the identified clusters present in a wide size range, indicating the inhomogeneity of the hybrid binder.

The measured porosity in Fig. 13a is in good agreement with the SEM observation that poor reaction in 6 % Na_2O samples results in a high porosity as compared to the high Na_2O% samples. There is no obvious trend in the change of porosity as Ms increases from 1.0 to 1.8. But in terms of 8 % Na_2O addition, an increase of porosity along with Ms. is detected, which might be related to the server cracking that is noticed in SEM micrographs (Fig. 13d-f). This is further verified by the pore size distribution (PSD) obtained from MIP results. As shown in Fig. 13b, the pores are classified as gel pores (≤10 nm), capillary pores (10–50 nm), and macropores (>50 nm) [64]. Under a low Na_2O of 6 %, with a higher Ms., the PSD follows a trend that the majority of pores transform from macropores to capillary/gel pores. As suggested by Duxson et al. [65] and Zheng et al. [66], with the increase of the binder Si/Al ratio, the pores are refined thanks to the increased gel formation. Accordingly, in 8 % Na_2O samples, the gel pores are largely increased with lowered macropores, which has been linked to the promoted gel formation. However, contrary to 6 % Na_2O samples, a lower capillary but higher macropore is noticed with higher Ms. This is in accordance with the SEM analysis that severer incompatibility of two types of gel leads to cracking and enlarges the thin capillaries to macropores/defects.

The compressive strength of the samples at the age of 7 and 28 days are depicted in Fig. 14. It is clear that Na content plays an important role in the compressive strength of AAFL, which increases significantly with a higher Na_2O%, and N8S1.0 exhibits the highest compressive strength of 37.89 MPa. This is in good agreement with the isothermal calorimetric, TG, and XRD results that a higher content of OH^- promotes the hydration reaction by increasing the dissolution of precursors, hence resulting in higher mechanical strength. At different Na_2O percentages, an opposite trend is detected in compressive strength evolution from 7 to 28 days as a function of Ms. With 6 % of Na_2O, a higher Ms. leads to increased compressive strength that is in line with the results presented in reaction kinetics. On the contrary, at a higher Na_2O percentage of 8 %, the compressive strength at 7 and 28 days decrease with a higher Ms. Two possible causes should be noted here: i) The main reason lies in the incompatibility between the two types of gel. According to XRD-Rietveld and SEM-EDX results, a higher Ms. further stimulates the dissolution of LS for calcium-enriched phases formation, hence intensifying the incompatibility between geopolymeric gel and calcium enriched gel, resulting in the formation of more cracks, as evidenced by SEM and MIP results. ii) Chemically, the highest cumulative heat release and thermalgravimetric mass loss are observed with the lowest Ms. This is suggested to arise from, at a higher Na_2O percentage, the excessive SiO_2 species from both precursors and activator could transform to polymerized SiO_4 that eventually precipitate, which in turn hinder the formation of geopolymeric gels [67]. The N8S1.0 sample possibly reaches a balance between the erosion of OH- and absorption of soluble silicates, thus achieving the highest reaction degree and compressive strength. As a result, the compressive strength is decreased with a higher Ms. at 8 % of Na_2O. Notably, the strength variation is insignificant from 7 to 28 days when taking the test deviation into the consideration. According to a previous study [28], the possible conversion reaction between calcium aluminate hydrates is largely hindered within the geopolymer system. Thus, the observed strength evolution is most likely to be related to the gel incompatibility mentioned above and/or micro-cracking due to drying shrinkage within alkaline activated binder.

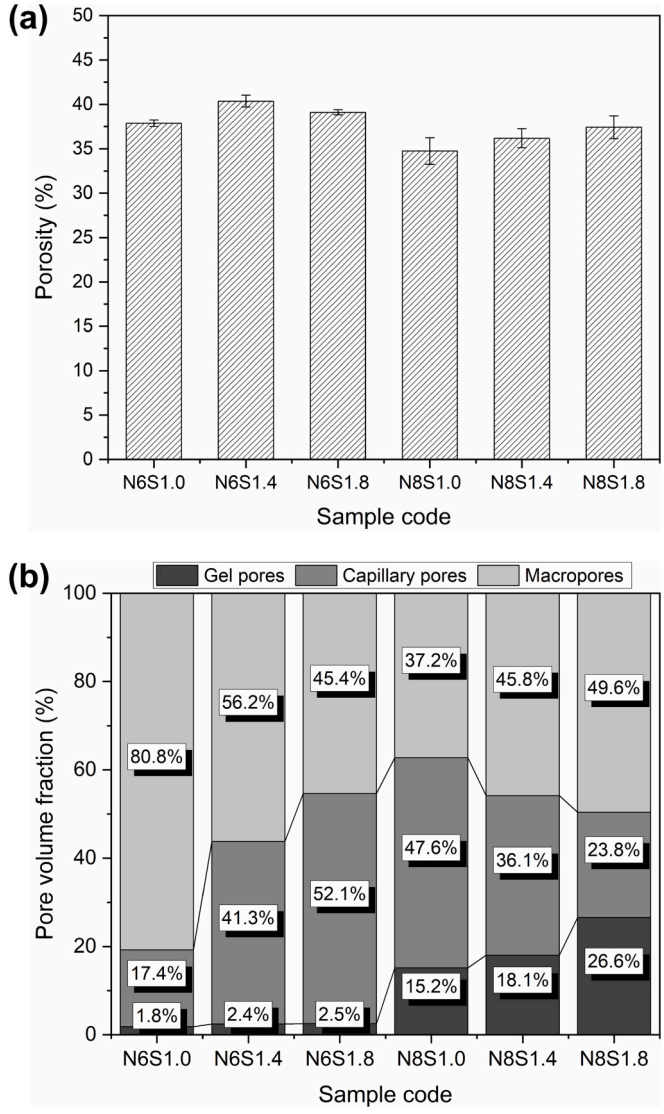

Fig. 13. The pore structure of samples with varied Na_2O% and Ms., (a) measured porosity, and (b) pore volume fraction obtained from MIP.

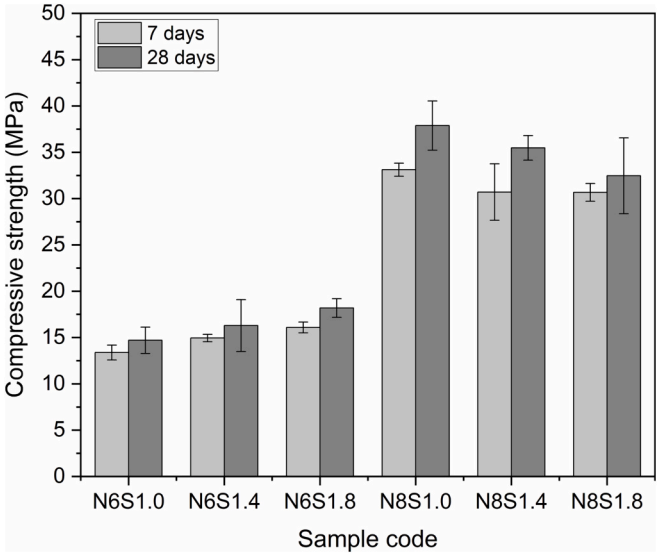

Fig. 14. Compressive strength and growth rate of samples between 7 and 28 days, with different Na_2O% and activator modulus.

3.5. High temperature behavior

After the systematic study of initial properties, the high temperature behavior of samples, including crystalline phase transformation as well as physical change of samples exposed to 800 °C, are investigated, and their synergetic influence on mechanical performance is assessed.

The XRD patterns of different mixtures after 800 °C are characterized and shown in Fig. 15. It can be observed that, as compared to the XRD patterns in Fig. 9, the initial mineralogical phase hydrogarnet disappears in all samples upon exposure to 800 °C, attributed to its dehydroxylation at around 300 °C, as evidenced by TG results. The amorphous hump centred around 30°-40° 2θ is becoming insignificant after 800 °C exposure. In addition, new crystalline phases including Akermanite-gehlenite ($Ca_2(Mg_{0.5}Al_{0.5})(Si_{1.5}Al_{0.5}O_7)$), Nepheline ($Na_{6.65}Al_{6.24}Si_{9.76}O_{32}$) and wollastonite-2 M ($CaSiO_3$) are noticed in all samples. Here, as triggered by high temperature, calcium enriched aluminosilicate gel (C-(N)-A-S-H) is decomposed and recrystallized into akermanite-gehlenite, and sodium enriched aluminosilicate gels (N-(C)-A-S-H) partially undergoes recrystallization, forming nepheline [13], while wollastonite-2 M is thermally formed from amorphous calcium silicates [68], which further explains the weakening of the amorphous hump. The presence of akermanite-gehlenite and nepheline phases correlates well with the results in gel compatibility characterization, further revealing the co-existence of geopolymeric gel and calcium enriched aluminosilicate gel (C-(N)-A-S-H).

When comparing the peaks of newly formed crystalline phases in the zoomed XRD diffractogram, intensified peaks of akermanite-gehlenite, nepheline, and wollastonite-2 M are noticed with higher Na_2O%. This indicates that Na content promotes the degree of thermal crystallization. Moreover, interestingly, for both samples with 6 % and 8 % of Na_2O, a higher Ms. has a negative influence on the thermal crystallization of akermanite-gehlenite and nepheline, especially for the sample with a higher Na_2O%. Here, the re-crystallization degree of geopolymers at elevated temperatures is highly related to the chemical composition of gel phases. Klima et al. [69] and Pan et al. [70] reported that Na dosage can lower the onset melting temperature of the amorphous phase, which has a direct influence on the re-crystallization degree. However, as for silicon, a similar phenomenon has been reported in sole fly ash based geopolymer [71,72] that the intensity of the nepheline phase is reduced with increasing silica modulus. In this study, it can be deduced that Si content has a negative influence on both sodium- and calcium-enriched crystalline phase formation at elevated temperatures. As a result, the detected thermal induced re-crystallization would inevitably vary the high temperature performance of geopolymers.

As shown in Fig. 16, the linear shrinkage of samples after 800 °C exposure is determined. A clear trend is detected that the thermally induced linear shrinkage is reduced with increasing Ms. as well as Na_2O %. Ms. has a dominant influence on the high Na sample, where increasing Ms. significantly lowers the linear shrinkage with the lowest shrinkage of 1.04 % achieved in the N8S1.8 sample. In general, the

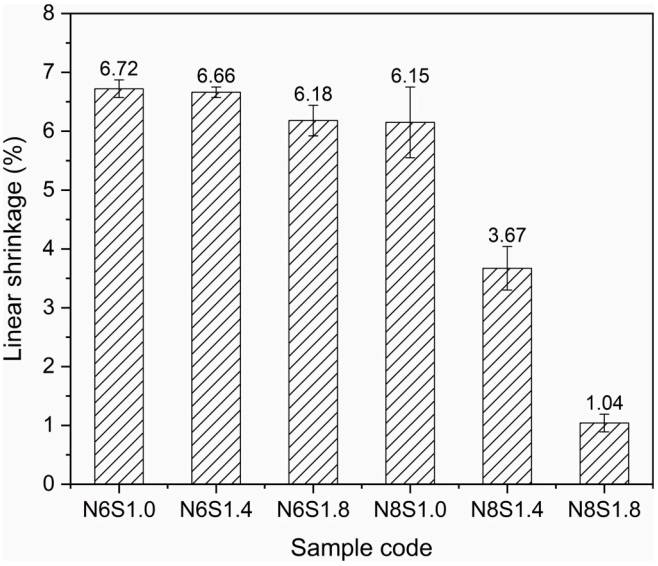

Fig. 16. The linear shrinkage of samples after high temperature exposure.

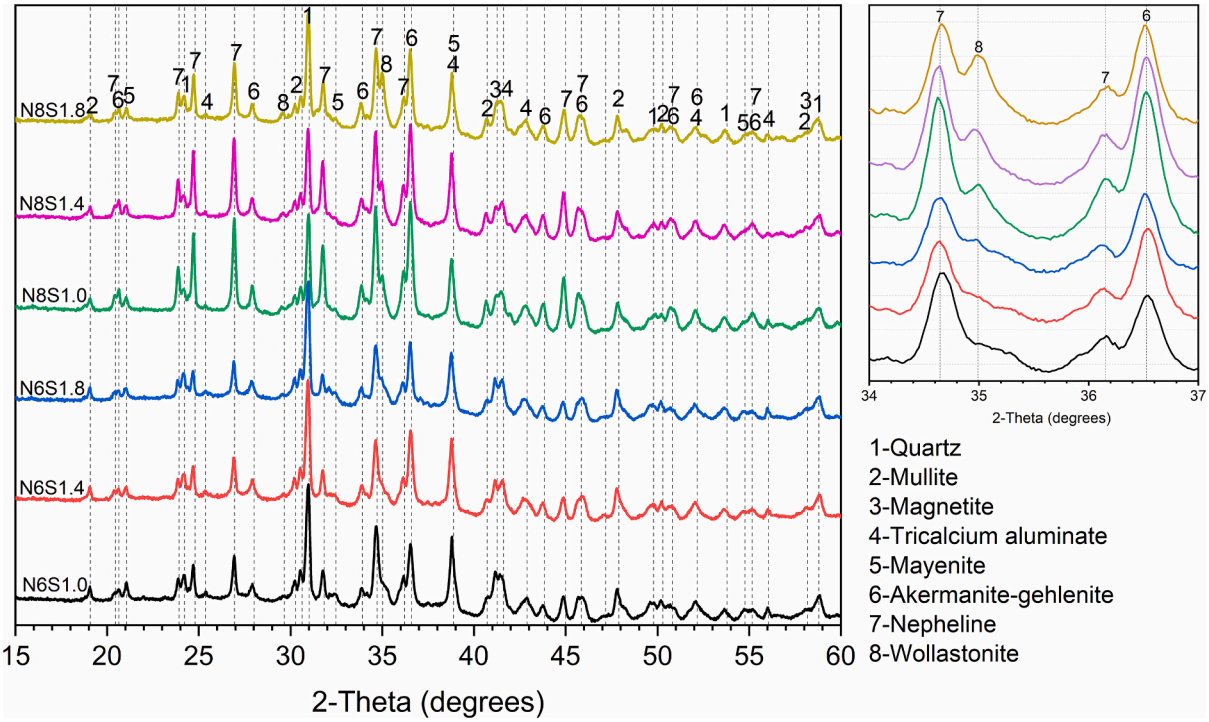

Fig. 15. XRD patterns of samples after high temperature exposure.

thermally induced volumetric change of hybrid geopolymers is mainly influenced by water evaporation (pore collapse), further geopolymerization (matrix densification), thermal incompatibility between different gels and their deterioration (cracking), crystallization and sintering, from room temperature to 800 °C [38]. Two linear shrinkage behaviours are differentiated in 6 % and 8 % Na_2O samples.

i) At a low Na_2O%, the matrix exhibits a typical geopolymeric behavior at elevated temperatures. This is because, under this situation, the reaction degree of the precursor is relatively low, hence the further geopolymerization as well as the vicious sintering play a leading role, which increases the matrix densification and thermal shrinkage. In this case, a higher Ms. promotes the reaction degree as evidenced by the increased mechanical strength, thereafter, weakening the further geopolymerization of remanent FA, resulting in a smaller thermal shrinkage.
ii) At a high Na_2O% of 8 %, the thermal behavior is impacted not only by geopolymeric gel but also Ca-enriched gel. The lower shrinkage in 8 % of Na_2O samples is suggested to partially arise from the high stiffness matrix owing to the promoted reactivity. Moreover, the highly dispersed dense Ca enrich gel and its re-crystalline phases at 800 °C can act as reinforcing backbone/aggregate to offer a certain degree of resistance to the thermally induced deformation [73]. In this case, the significant reduction in thermal shrinkage with increasing Ms. is highly related to the stimulated Ca-enriched gel formation. Simultaneously, as aforementioned, with a higher Ms., the microcracks formed due to the incompatibility between different gels facilitate water evaporation at high temperatures, contributing to reduced thermal deformation.

More detailed information on microstructural change due to high temperature is disclosed by MIP. The PSD before and after high temperature exposure is compared in Fig. 17. For samples with 6 % of Na_2O, as compared to the PSD at room temperature, the main peak below 500 nm transforms to a larger size fraction after 800 °C. This transformation is because of the healing of small pores and defects by further geopolymerization and sintering, as well as the crack formation induced by the thermal degradation of gels. When increasing Ms., the peak of the main pore fraction is stably centred at around 2000–3000 nm with a higher intensity. Here, the intensified peak with increasing Ms. indicates the declined geopolymeric behavior as discussed above. A similar transformation of the main pore size fraction is also observed in samples with higher Na_2O percentage, which however shifts to a larger pore size diameter. But there is no obvious trend in main peak intensity variation, except the main pore fraction peak shifts from 5000 nm to 8000 nm with a higher Ms. Here, the enlarged pore size should be a result of either the discrepant expansion behavior between geopolymer gel and Ca-enriched gel or the severe thermal degradation of hydrated products, mainly Ca-enriched gels. In addition, it is worth noting that N8S1.0 has the highest fraction of pores larger than 100 μm after high temperature exposure as an indicator of increased macrocracks.

The residual compressive strength of samples after 800 °C is compared with the initial strength in Fig. 18a and the strength change ratio is calculated. As discussed above, the distinctly different thermal evolution phenomenon observed in samples with varied Na_2O% has posed a direct influence on mechanical strength evolution under high temperatures. Among these, the samples with low Na_2O% undergo an obvious strength gain at a rate from 212 % to 441 %, as compared to the strength gain up to 20 % in the samples with high Na_2O% after elevated temperature exposure. Here the mechanical strength evolution patterns can be classified into:

(1) Geopolymer pattern (Low Na_2O%)

Geopolymer dominated pattern exhibited a typical thermal behavior of geopolymer binder, with the most distinctive feature of large strength

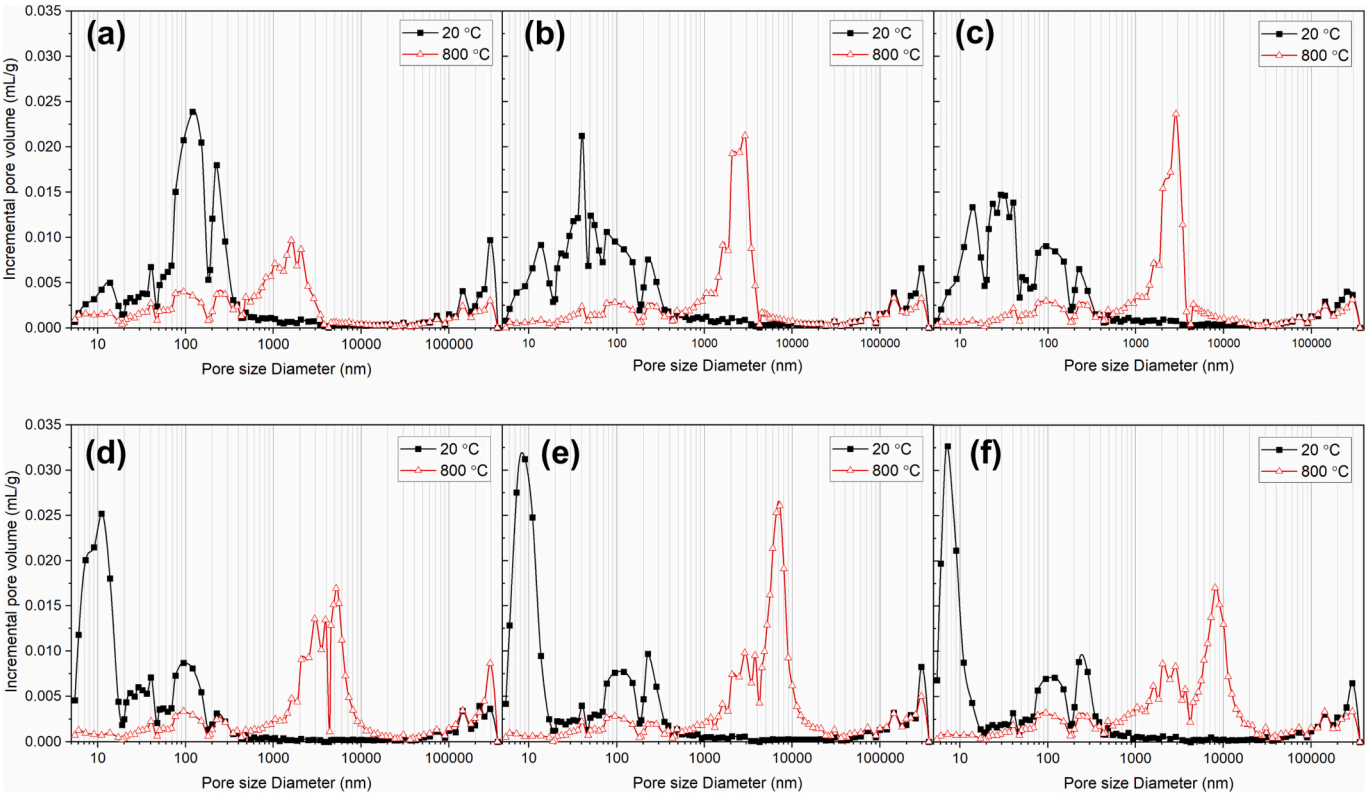

Fig. 17. The pore structural transformation of samples before and after high temperature exposure, (a) - (f) represent N6S1.0, N6S1.4, N6S1.8, N8S1.0, N8S1.4, N8S1.8 respectively.

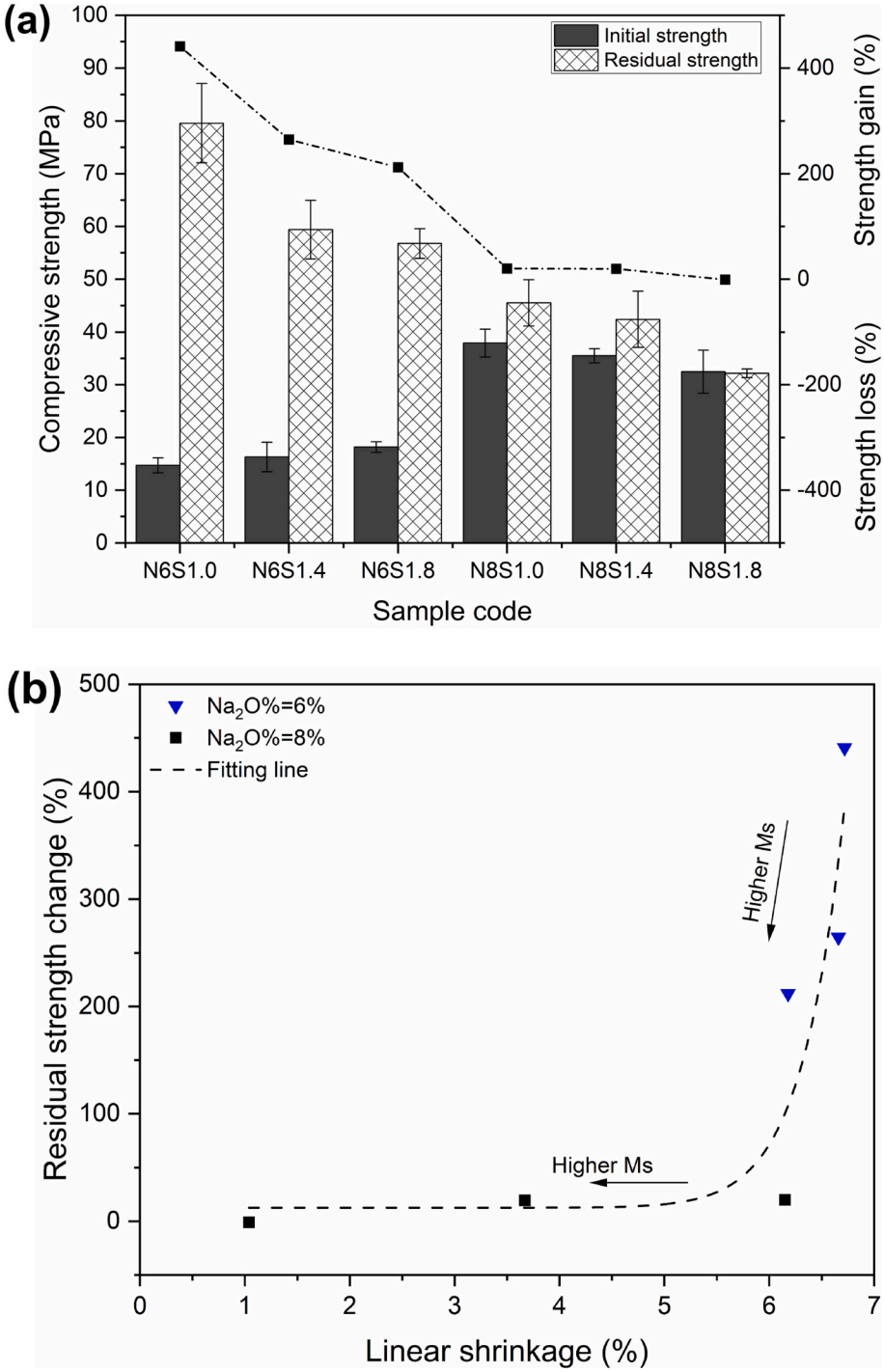

Fig. 18. (a) The compressive strength of samples before and after thermal exposure, (b) The relationship between linear shrinkage and residual strength.

gain upon exposure to high temperatures. A lower Na_2O% leads to a higher proportion of geopolymeric gel compared to Ca-enriched gel, resulting from the low reaction degree. Hence, further geopolymerization and vicious sintering play the leading role at elevated temperatures. It leads to high thermal shrinkage with large strength gain. While the increasing Ms. is proved to lower the thermally induced matrix densification, thereafter, resulting in a reduction of strength gain ratio.

(2) Hybrid gel pattern (High Na_2O%)

This thermal strength evolution pattern in the hybrid gel system is either differentiated from geopolymeric binder or Ca-dominated binder, which exhibits good mechanical stability with slight strength gain/loss and a tolerable shrinking percentage after high temperature exposure. Here, the further reaction of geopolymer gel and degradation of Ca-enriched gel simultaneously govern the thermal mechanical evolution. On the one hand, the boosted activation degree results in a high stiffness matrix with reduced capacity to accommodate thermal incompatibilities, thus weakening the strength gain at high temperatures [70,74]. On the other hand, it is known that, as compared to geopolymeric gel with superior thermal stability, C-A-S-H gel decomposes from 400 °C to 600 °C and fully crystallizes at 800 °C [20,38], inevitably leading to matrix deterioration. Under the coupling effect of two gels, a

relatively small strength gain is observed at high temperatures.

The strength evolution and linear shrinkage under high temperature is further correlated in Fig. 18b. In general, the linear shrinkage is decreasing with the residual strength gain ratio. But it is worth noting that the change of strength gain ratio also follows two different trends. At a low Na_2O%, the residual strength change ratio responds rapidly from 212.1 % to 441.0 % as linear shrinkage increases from 6.1 % to 6.7 %, while at a higher Na_2O%, the change ratio slowly increases from −1.0 % to 20.1 % when linear shrinkage increases from 1.0 % to 6.2 %. It indicates the thermal strength evolution is not fully predominated by matrix densification/shrinkage, especially for hybrid gel systems. In a hybrid gel system, increasing Ms. promotes the reaction of LS to form C-A-(*S*)-H gel, which causes a tendency of cracking at high temperatures, thus weakening the densification effect raised from geopolymeric gel. With the highest Ms. of 1.8, it is believed that the thermal responses of two gels reach a balance, hence a minor shrinkage with small strength variation is achieved.

4. Discussion

4.1. The calcium availability in determining geopolymer gel composition and reaction mechanism

In this study, the highly crystalline LS is incorporated as a Ca source in the hybrid geopolymer system. An alkali activator with a specific Na_2O percentage and silica modulus is applied. The results testify that Na_2O% has a more significant influence on the reaction mechanism as compared to Ms., as reflected in raw materials dissolution, reaction kinetics, and binder gel assemblage. The above characterization and results are combined to provide a mechanistic understanding on the case of low Ca availability in determining hybrid geopolymer gel composition, as shown in Fig. 19.

For the initial stage in Fig. 19a, the rapid hydration of $C_{12}A_7$ and C_3A in LS surpasses FA, and initiates a quick polycondensation, resulting in a significantly shortened setting and lower flowability as compared to sole FA-based geopolymer. With continuous dissolution and reaction of LS, a layer of calcium aluminate hydrates is preferentially formed on the surface of unreacted LS grain as observed by SEM (See Figs. 10, 12), which has been previously reported in LS and calcium aluminate based systems [59,75–78]. This is similar to OPC system, but the higher content of calcium aluminates (C_3A and $C_{12}A_7$) presented in LS initiates more rapid initial hydration. Thus, the Ca in LS is largely consumed as soon as it contacts with water to form the calcium aluminate hydrates layer, and the formed layer further restricts the mutual diffusion of environmental reactant species (alkali activator) as well as the dissolved ions [78], resulting in a low environmental Ca availability. This limited ion diffusion phenomenon through the product layer is verified by the ion proportion balance among the two gels discussed in Section 3.3.

Owing to that, the slow Ca^{2+} diffusion into the environment results in a minor substitution of Na^+ in N-A-S-H gels by Ca^{2+} rather than geopolymerization interruption, hence resulting in a N-(C)-A-S-H phase as observed in Fig. 11. Notably, in this case, the 3D aluminosilicate framework is retained, which can be distinguished from the 2D C-A-S-H gel as reported by García-Lodeiro et al. [16,61]. Hence the resultant geopolymeric binder shows certain thermal stability. Simultaneously, the environmental species such as Na^+, $Si(OH)_4$ can in turn, diffuse into the layer to be absorbed into calcium aluminate hydrates. Thus, a Na and Si substituted calcium aluminate hydrate (C-(N)-A-(*S*)-H) is characterized in SEM/EDX results. It is worth noting that, since the thickness of product layers keeps increasing and the continuous consumption of alkali, the ion diffusion as well as the reaction of LS are eventually restricted or hindered, resulting in the clustered areas consisting of unreacted LS and hydrated C-(N)-A-(*S*)-H type gel. As a result, a hybrid binder with clustered Ca-enriched gel (C-(N)-A-(*S*)-H) wrapping around geopolymeric gel (N-(C)-A-S-H) is observed. Among these, a higher Na_2O% or Ms. can promote the reaction of LS, thus governing the co-existence of two gels, which will be discussed in the following section.

In conclusion, calcium availability, including calcium release rate and release degree, plays a prevalent role in determining geopolymer gel composition. The commonly used secondary Ca precursor in geopolymers, for instance, GGBFS, and OPC, leads to rapid/high amorphous Ca supply, which largely accelerates the hydration degree but also impedes the formation of geopolymeric gel (N-A-S-H), resulting in a Ca dominated binder [79,80]. While for precursors with limited Ca availability, such as LS, the limitation on the Ca diffusion under alkali activation results in a unique reaction pathway, where a low Ca release rate into the environment relative to the geopolymeric reaction would not interfere with either the formation or the microstructure of N-A-S-H gel. With a partial ion exchange between Na^+ and Ca^{2+}, a hybrid binder consisting of isolated C-(N)-A-(*S*)-H type gel and N-(C)-A-S-H type gel is resulted.

4.2. The compatibility between N-A-S-H and C-A-S-H gel

This study provides new insights into the phase compatibility in alkali activated slag/FA blends and its influence on room-high temperature behavior. A conceptual model is proposed based on the present results, as shown in Fig. 20. At a low Na_2O%, the limited dissolution and

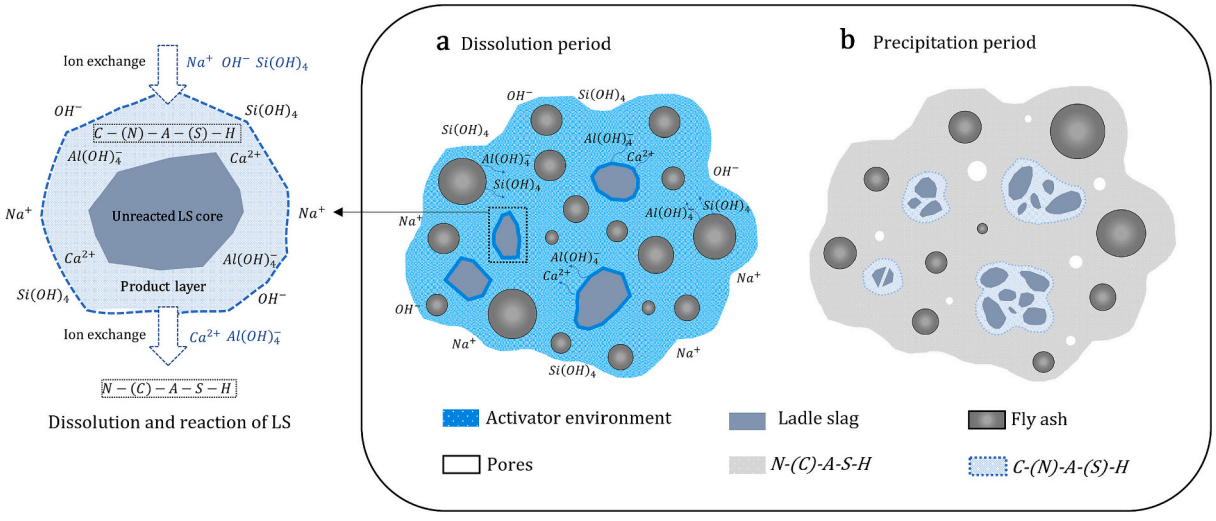

Fig. 19. Schematic representation of reaction mechanism between LS and FA under alkali-activation.

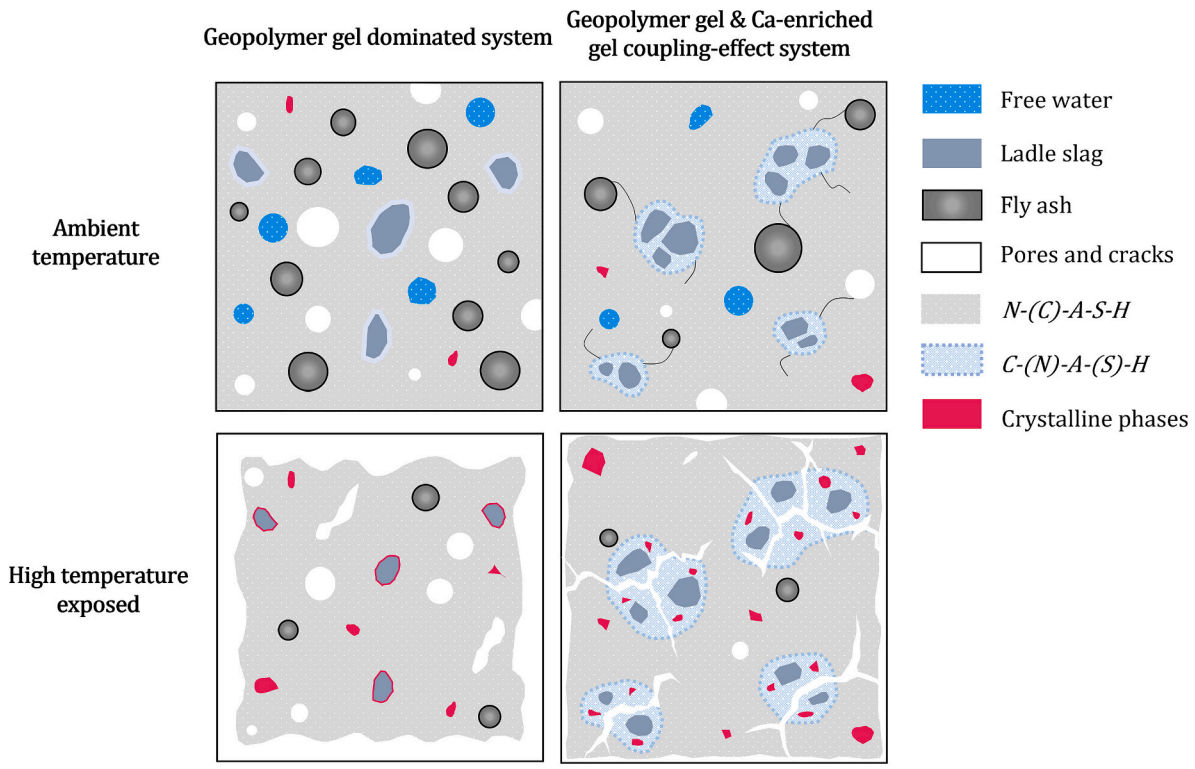

Fig. 20. Comparative conceptual model of the geopolymer gel dominated system, and geopolymer gel & Ca-enriched gel co-effect system, and the thermal degradation up to 800 °C.

reaction degree results in a loose matrix with abundant unreacted precursor particles. Moreover, with a relatively low alkaline concentration, only a thin hydrated layer formed on the surface of LS particles due to its low dissolution and reaction degree. Hence the sample is dominated by a geopolymer gel, exhibiting a high porosity and low mechanical strength. Under the condition with high Na_2O%, the increased alkaline concentration promotes the dissolution of precursors, leading to better workability. On the one hand, more FA particles are reacted for geopolymer gel formation. On the other hand, with an enhanced dissolution, the product shell of LS keeps growing until the cease of LS reaction and ion exchange. As a result, two hydrated gels, namely C-(N)-A-(*S*)-H type gel and N-(C)-A-S-H type gel develop simultaneously in a relatively dense matrix, achieving a low porosity and high mechanical strength as compared to geopolymer gel dominated binder. In addition, according to the XRD and SEM-EDX results, increasing Ms. further promotes the dissolution as well as the reaction degree of precursors. It intensifies the incompatibility between geopolymer gel and Ca-enriched gel, giving rise to microcrack formation along the boundary between two gels, as evidenced by the SEM and MIP analyses. Therefore, a lower mechanical strength is obtained along with the increasing Ms. The discrepancy between the geopolymer gel dominated system and geopolymer gel & Ca-enriched gel coupling-effect system presents interesting characteristics under high temperatures, which are discussed below:

(a) Geopolymer gel dominated system.

As presented in Fig. 20, upon 800 °C exposure, most remanent FA particles further react to form geopolymer gel, and the free water is evaporated. The viscous sintering of geopolymer gel at around 800 °C fills small pores and heals microcracks. Moreover, the Ca-enriched gel is prone to dehydrate/decompose at intermediate temperature and fully recrystallize at 800 °C, which leads to strength deterioration and crack formation. However, in our previous study [28], the low content of C-A-S-H gel due to the low reaction degree has a limited adverse effect on high temperature behavior. Meanwhile, the calcium induced crystalline phases, such as akermanite and gehlenite further strengthen the matrix as reported by [70,71]. These phenomena predominate in the thermal behavior, which contributes to matrix densification with high shrinkage. As a result, a large strength gain is observed in the geopolymer dominated system.

(b) Geopolymer gel & Ca-enriched gel coupled system.

The proposed reaction mechanism results in the co-existence of two separate gels within the matrix, enabling a coupling effect of geopolymer gel and Ca-enriched gel under high temperatures. On the one hand, as mentioned above, the further geopolymerization along with viscous sintering leads to the densification of the matrix by healing small pores and cracks, while posing a tendency for shrinking. On the other hand, the dense Ca-enriched gel and its thermally induced crystalline phases show certain resistance to thermal shrinkage with crack formation as observed in MIP results. In addition, the crack formation because of gel incompatibility is believed to ease thermal stress by acting as a transport channel for water evaporation. Above all, the different thermal behaviors between geopolymeric gel and Ca-enriched gel have a combined effect in determining the thermal performance of the resultant binder. This explains the insignificant linear shrinkage and compressive strength change observed in the sample with high Na_2O% and Ms. after high temperature exposure (See Fig. 19). According to the proposed model, it is possible to design a hybrid geopolymer with desired volumetric and mechanical stability under elevated temperatures by tailoring the two competing mechanisms. Nevertheless, to achieve an optimum thermal stability, a high alkali content is applied in this work. Further investigation is necessary to explore alternative solutions that utilize low/non-alkali activators to realize eco-friendly applications for high temperature resistant geopolymers.

5. Conclusions

In the current study, the role of Ca availability in determining the gel compatibility of calcium incorporated geopolymers is revealed. Ladle slag and Class F fly ash in a blended ratio of 2:8 is subjected to the alkali activator with different compositions. The reaction mechanism and gel compatibility are investigated, and their further influence on physico-chemical properties and thermal behavior is determined. The experimental results lead to the following conclusions:

- The activator composition of Na_2O% and silica modulus (Ms) has a direct influence on the dissolution and hydration of LS. Among these, sodium dosage has a more significant impact on hybrid binder over Ms., reflected by precursors dissolution, workability, reaction kinetics, and binder gel assemblage. A higher Na_2O% contributes to better workability and promotes the dissolution of raw precursors. Increased Ms. stimulates the dissolution and hydration of calcium aluminate phases, and leads to a higher level of silica cross-linking in aluminosilicate gel.
- The availability of environmental Ca plays a vital role in determining the gel composition of AAFL blends. With continuous dissolution and the reaction of LS, a product layer is formed on the surface of slag particles due to the hydration of calcium aluminates, which strongly limits the further Ca dissolution and diffusion into the environment. The limited Ca availability (small amount and/or slow Ca diffusion rate) retains the geopolymerization, with the formation of a partial Ca uptake N-A-S-H gel, preserving the 3D framework of geopolymer. As a result, two hydrated gels, namely C-(N)-A-S-H type gel and N-(C)-A-S-H type gel, are developed separately in a hybrid binder.
- For the alkali activated FA/LS system, the incompatibility between two gels is insignificant at a relatively low Na dosage, which remains to be a geopolymer gel dominated system. However, with a promoted reaction degree at higher Na_2O%, a structure with clustered Ca-enriched gel (C-(N)-A-(*S*)-H) wrapping around geopolymeric gel (N-(C)-A-S-H) is obtained, achieving a dense matrix with low porosity and high mechanical strength as compared to geopolymer gel dominated binder. Moreover, at this condition, a higher Ms. intensifies the incompatibility between geopolymer gel and Ca-enriched gel, giving rise to microcrack formation along the boundary between the two gels. Therefore, increased porosity and decreased mechanical strength are resulted.
- A new thermal behavior pattern ruled by the simultaneous effect of geopolymeric gel and Ca-enriched gel is uncovered. At high temperatures, there is a combined phenomenon among the different thermal behavior between geopolymeric gel and Ca-enriched gel in determining the thermal performance of the resultant matrix. This finding helps to design hybrid geopolymers with desired volumetric and mechanical stability at elevated temperatures by tailoring the relative intensity between the two competing mechanisms.

CRediT authorship contribution statement

Y. Luo: Methodology, Investigation, Data curation, Formal analysis, Validation, Writing – original draft. **H.J.H. Brouwers:** Funding acquisition, Supervision, Writing – review & editing. **Qingliang Yu:** Conceptualization, Supervision, Funding acquisition, Project administration, Writing – review & editing.

Declaration of competing interest

The authors declare that they have no known competing financial interests or personal relationships that could have appeared to influence the work reported in this paper.

Data availability

Data will be made available on request.

Acknowledgments

This research is carried out under China Scholarship Council (No. 201906370011) and the Department of the Built Environment at Eindhoven University of Technology. The authors wish to thank Prof. Dr. S.R. van der Laan (Tata Steel, The Netherlands) for the Ladle slag supply. The authors gratefully acknowledge Dr. K. Schollbach (Eindhoven University of Technology, The Netherlands) for her help with PARC analysis. Special thanks are given to Weitan Zhuang (Wuhan University, China) for assistance with MIP measurements.

Appendix

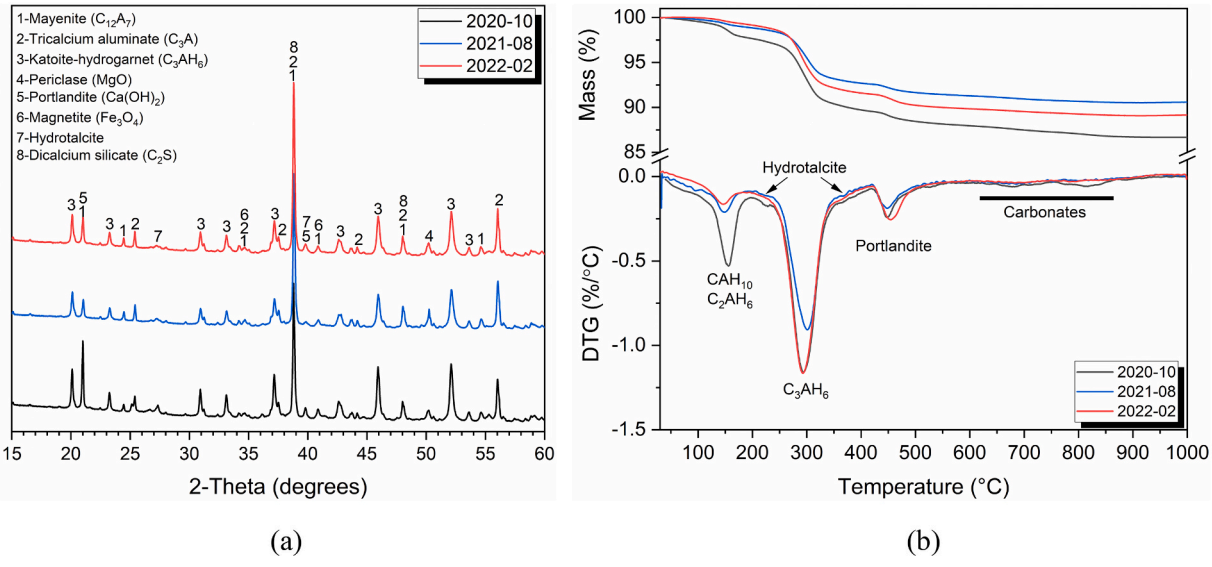

Fig. A1. The variability between raw ladle slag collection from 2020 to 2022, (a) XRD patterns and (b) TGA-DTG results.

Table A1
The average chemical composition of phases calculated by PARC.

Phase	Oxide											
	Na_2O	MgO	Al_2O_3	SiO_2	P_2O_5	SO_3	K_2O	CaO	TiO_2	MnO	Fe_xO_y	NiO
C-(N)-A-S-H	2.21	1.06	22.10	22.79	1.66	1.43	0.39	44.63	–	0.83	1.59	1.30
N-(C)-A-S-H	13.16	0.50	13.84	51.92	1.64	2.22	1.37	11.46	–	–	3.90	–
Mullite	2.19	1.05	29.33	53.72	1.46	1.43	2.59	1.82	1.36	–	5.05	–
Quartz	1.73	0.19	2.07	88.97	1.95	2.47	–	0.43	0.30	–	1.89	–
CAs, CAH	0.37	0.65	34.14	1.52	0.99	1.12	–	59.52	–	0.70	0.98	–
FexOy	–	1.24	2.62	1.47	1.05	0.19	0.06	0.49	0.20	1.31	91.38	–
Periclase	1.22	79.18	6.42	2.47	0.00	0.00	0.85	0.85	0.03	2.58	6.39	–
C_2S	1.74	–	3.92	25.38	2.34	0.59	0.10	43.00	0.70	0.04	21.25	0.94

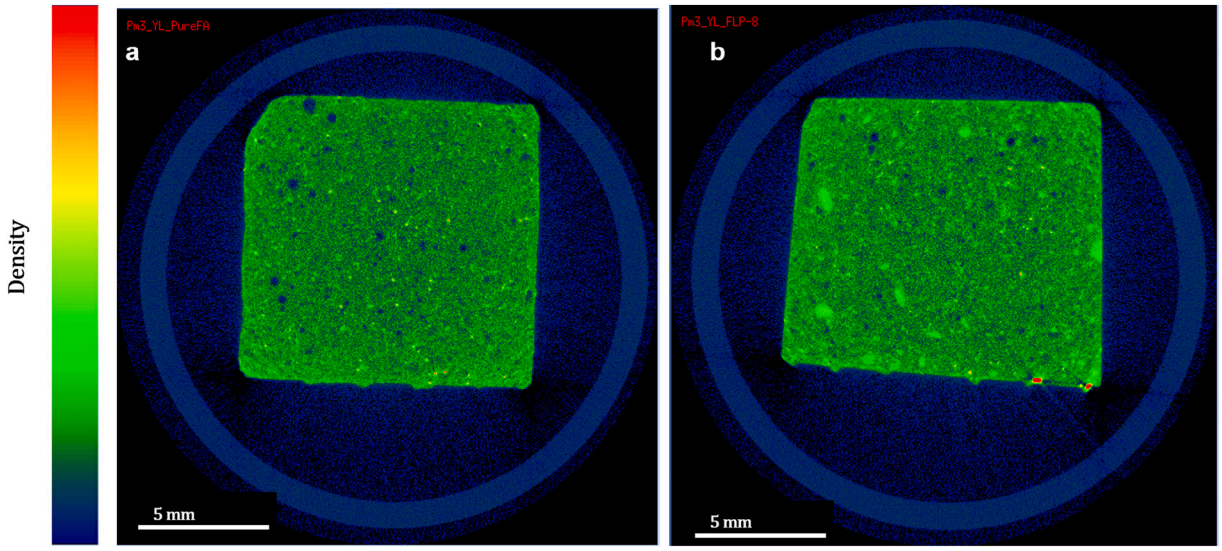

Fig. A2. Comparison between Micro-CT 2D images depending on density, a) Plain FA based geopolymer, b) LS/FA hybrid geopolymer.

References

[1] J.L. Provis, Alkali-activated materials, Cem. Concr. Res. 114 (2018) 40–48, https://doi.org/10.1016/j.cemconres.2017.02.009.
[2] J.L. Provis, A. Palomo, C. Shi, Advances in understanding alkali-activated materials, Cem. Concr. Res. 78 (2015) 110–125, https://doi.org/10.1016/j.cemconres.2015.04.013.
[3] J.L. Provis, Geopolymers and other alkali activated materials: why, how, and what? Mater. Struct. 47 (2014) 11–25, https://doi.org/10.1617/s11527-013-0211-5.
[4] J. Zhao, L. Tong, B. Li, T. Chen, C. Wang, G. Yang, Y. Zheng, Eco-friendly geopolymer materials: a review of performance improvement, potential application and sustainability assessment, J. Clean. Prod. 307 (2021), 127085, https://doi.org/10.1016/j.jclepro.2021.127085.
[5] P. Duxson, A. Fernández-Jiménez, J.L. Provis, G.C. Lukey, A. Palomo, J.S.J. van Deventer, Geopolymer technology: the current state of the art, J. Mater. Sci. 42 (2007) 2917–2933, https://doi.org/10.1007/s10853-006-0637-z.
[6] M. Lahoti, K.H. Tan, E.-H. Yang, A critical review of geopolymer properties for structural fire-resistance applications, Constr. Build. Mater. 221 (2019) 514–526, https://doi.org/10.1016/j.conbuildmat.2019.06.076.
[7] T. Bakharev, Resistance of geopolymer materials to acid attack, Cem. Concr. Res. 35 (2005) 658–670, https://doi.org/10.1016/j.cemconres.2004.06.005.
[8] J.G.S.Van Jaarsveld, J.S.J.Van Deventer, A. Schwartzman, The potential use of geopolymeric materials to immobilise toxic metals: Part II. Material and leaching characteristics, Minerals Engineering. 12 (1999) 75–91, https://doi.org/10.1016/S0892-6875(98)00121-6.
[9] C. Li, H. Sun, L. Li, A review: the comparison between alkali-activated slag (Si+Ca) and metakaolin (Si+Al) cements, Cem. Concr. Res. 40 (2010) 1341–1349, https://doi.org/10.1016/j.cemconres.2010.03.020.
[10] C.K. Yip, G.C. Lukey, J.S.J. van Deventer, The coexistence of geopolymeric gel and calcium silicate hydrate at the early stage of alkaline activation, Cem. Concr. Res. 35 (2005) 1688–1697, https://doi.org/10.1016/j.cemconres.2004.10.042.
[11] I. García-Lodeiro, A. Fernández-Jiménez, A. Palomo, Variation in hybrid cements over time. Alkaline activation of fly ash–portland cement blends, Cem. Concr. Res. 52 (2013) 112–122, https://doi.org/10.1016/j.cemconres.2013.03.022.
[12] M.L. Granizo, S. Alonso, M.T. Blanco-Varela, A. Palomo, Alkaline activation of metakaolin: effect of calcium hydroxide in the products of reaction, J. Am. Ceram. Soc. 85 (2002) 225–231, https://doi.org/10.1111/j.1151-2916.2002.tb00070.x.
[13] S.M. Park, J.G. Jang, N.K. Lee, H.K. Lee, Physicochemical properties of binder gel in alkali-activated fly ash/slag exposed to high temperatures, Cem. Concr. Res. 89 (2016) 72–79, https://doi.org/10.1016/j.cemconres.2016.08.004.
[14] I. Ismail, S.A. Bernal, J.L. Provis, R. San Nicolas, S. Hamdan, J.S.J. van Deventer, Modification of phase evolution in alkali-activated blast furnace slag by the incorporation of fly ash, Cem. Concr. Compos. 45 (2014) 125–135, https://doi.org/10.1016/j.cemconcomp.2013.09.006.
[15] C.K. Yip, G.C. Lukey, J.L. Provis, J.S.J. van Deventer, Effect of calcium silicate sources on geopolymerisation, Cem. Concr. Res. 38 (2008) 554–564, https://doi.org/10.1016/j.cemconres.2007.11.001.
[16] I. García-Lodeiro, A. Fernández-Jiménez, A. Palomo, D.E. Macphee, Effect of calcium additions on N-A–S–H cementitious gels, J. Am. Ceram. Soc. 93 (2010) 1934–1940, https://doi.org/10.1111/j.1551-2916.2010.03668.x.
[17] S.A. Bernal, R.M. de Gutiérrez, F. Ruiz, H. Quiñones, J.L. Provis, High-temperature performance of mortars and concretes based on alkali-activated slag/metakaolin blends, Mater. Constr. 62 (2012) 471–488, https://doi.org/10.3989/mc.2012.01712.
[18] S.A. Bernal, E.D. Rodríguez, R. Mejía de Gutiérrez, M. Gordillo, J.L. Provis, Mechanical and thermal characterisation of geopolymers based on silicate-activated metakaolin/slag blends, J. Mater. Sci. 46 (2011) 5477–5486, https://doi.org/10.1007/s10853-011-5490-z.
[19] Z. Pan, Z. Tao, Y.F. Cao, R. Wuhrer, T. Murphy, Compressive strength and microstructure of alkali-activated fly ash/slag binders at high temperature, Cem. Concr. Compos. 86 (2018) 9–18, https://doi.org/10.1016/j.cemconcomp.2017.09.011.
[20] N.K. Lee, K.T. Koh, G.H. An, G.S. Ryu, Influence of binder composition on the gel structure in alkali activated fly ash/slag pastes exposed to elevated temperatures, Ceram. Int. 43 (2017) 2471–2480, https://doi.org/10.1016/j.ceramint.2016.11.042.
[21] O. Najm, H. El-Hassan, A. El-Dieb, Ladle slag characteristics and use in mortar and concrete: a comprehensive review, J. Clean. Prod. 288 (2021), 125584, https://doi.org/10.1016/j.jclepro.2020.125584.
[22] V.Z. Serjun, B. Mirti, A. Mladenovi, Evaluation of ladle slag as a potential material for building and civil engineering, Materiali in Tehnologije. 8 (2013).

[23] D. Adolfsson, R. Robinson, F. Engström, B. Björkman, Influence of mineralogy on the hydraulic properties of ladle slag, Cem. Concr. Res. 41 (2011) 865–871, https://doi.org/10.1016/j.cemconres.2011.04.003.
[24] C. Shi, Characteristics and cementitious properties of ladle slag fines from steel production, Cem. Concr. Res. 32 (2002) 459–462, https://doi.org/10.1016/S0008-8846(01)00707-4.
[25] A. Fernández-Jiménez, T. Vázquez, A. Palomo, Effect of sodium silicate on calcium aluminate cement hydration in highly alkaline media: a microstructural characterization, J. Am. Ceram. Soc. 94 (2011) 1297–1303, https://doi.org/10.1111/j.1551-2916.2010.04242.x.
[26] A. Fernández-Jiménez, Á. Palomo, T. Vazquez, R. Vallepu, T. Terai, K. Ikeda, Alkaline activation of blends of metakaolin and calcium aluminate, J. Am. Ceram. Soc. 91 (2008) 1231–1236, https://doi.org/10.1111/j.1551-2916.2007.02002.x.
[27] C. Pastor, A. Fernández-Jiménez, T. Vázquez, Á. Palomo, Calcium aluminate cement hydration in a high alkalinity environment, Mater. Constr. 59 (2009) 21–34, https://doi.org/10.3989/mc.2009.42407.
[28] Y. Luo, K.M. Klima, H.J.H. Brouwers, Q. Yu, Effects of ladle slag on class F fly ash geopolymer: reaction mechanism and high temperature behavior, Cem. Concr. Compos. 129 (2022), 104468, https://doi.org/10.1016/j.cemconcomp.2022.104468.
[29] N. Ukrainczyk, T. Matusinovic, S. Kurajica, B. Zimmermann, J. Sipusic, Dehydration of a layered double hydroxide—C2AH8, Thermochim. Acta 464 (2007) 7–15, https://doi.org/10.1016/j.tca.2007.07.022.
[30] E. Adesanya, H. Sreenivasan, A.M. Kantola, V.-V. Telkki, K. Ohenoja, P. Kinnunen, M. Illikainen, Ladle slag cement – characterization of hydration and conversion, Constr. Build. Mater. 193 (2018) 128–134, https://doi.org/10.1016/j.conbuildmat.2018.10.179.
[31] British Standards Institution, London, BS EN 1015-3: Methods of Test for Mortar for Masonry - Part 3: Determination of Consistence of Fresh Mortar (by Flow Table), 1999.
[32] British Standards Institution, Methods of Testing Cement. Part 3, 2016.
[33] C. van Hoek, J. Small, S. van der Laan, Large-area phase mapping using PhAse recognition and characterization (PARC) software, Microscopy Today. 24 (2016) 12–21, https://doi.org/10.1017/S1551929516000572.
[34] K. Scrivener, R. Snellings, B. Lothenbach (Eds.), A Practical Guide to Microstructural Analysis of Cementitious Materials, CRC Press, 2018, https://doi.org/10.1201/b19074.
[35] British Standards Institution, London, Methods of testing cement. Part 1, Part 1, 2016.
[36] F. Fan, Z. Liu, G. Xu, H. Peng, C.S. Cai, Mechanical and thermal properties of fly ash based geopolymers, Constr. Build. Mater. 160 (2018) 66–81, https://doi.org/10.1016/j.conbuildmat.2017.11.023.
[37] R. Cai, H. Ye, Clinkerless ultra-high strength concrete based on alkali-activated slag at high temperatures, Cem. Concr. Res. 145 (2021), 106465, https://doi.org/10.1016/j.cemconres.2021.106465.
[38] Y. Luo, S.H. Li, K.M. Klima, H.J.H. Brouwers, Q. Yu, Degradation mechanism of hybrid fly ash/slag based geopolymers exposed to elevated temperatures, Cem. Concr. Res. 151 (2022), 106649, https://doi.org/10.1016/j.cemconres.2021.106649.
[39] N. Hui-Teng, H. Cheng-Yong, L. Yun-Ming, M.M.A. Bakri Abdullah, C. Rojviriya, P. W. Ken, O. Shee-Ween, H. Yong-Jie, O. Wan-En, Thermo-mechanical behaviour of fly ash-ladle furnace slag blended geopolymer with incorporation of decahydrate borax, Constr. Build. Mater. 331 (2022), 127337, https://doi.org/10.1016/j.conbuildmat.2022.127337.
[40] P. Zhang, Y. Zheng, K. Wang, J. Zhang, A review on properties of fresh and hardened geopolymer mortar, Compos. Part B 152 (2018) 79–95, https://doi.org/10.1016/j.compositesb.2018.06.031.
[41] B. Sun, Y. Sun, G. Ye, G. De Schutter, A mix design methodology of slag and fly ash-based alkali-activated paste, Cem. Concr. Compos. 126 (2022), 104368, https://doi.org/10.1016/j.cemconcomp.2021.104368.
[42] C. Shi, D. Roy, P. Krivenko, Alkali-activated Cements and Concretes, CRC Press, London, 2014, https://doi.org/10.1201/9781482266900.
[43] A.M. Kaja, A. Lazaro, Q.L. Yu, Effects of Portland cement on activation mechanism of class F fly ash geopolymer cured under ambient conditions, Constr. Build. Mater. 189 (2018) 1113–1123, https://doi.org/10.1016/j.conbuildmat.2018.09.065.
[44] R. Dron, F. Brivot, Thermodynamic and kinetic approach to the alkali-silica reaction. Part 1: concepts, Cem. Concr. Res. 22 (1992) 941–948, https://doi.org/10.1016/0008-8846(92)90118-F.
[45] Z. Sun, A. Vollpracht, Isothermal calorimetry and in-situ XRD study of the NaOH activated fly ash, metakaolin and slag, Cem. Concr. Res. 103 (2018) 110–122, https://doi.org/10.1016/j.cemconres.2017.10.004.
[46] D. Adolfsson, R. Robinson, F. Engström, B. Björkman, Influence of mineralogy on the hydraulic properties of ladle slag, Cem. Concr. Res. 41 (2011) 865–871, https://doi.org/10.1016/j.cemconres.2011.04.003.
[47] S.A. Bernal, J.L. Provis, V. Rose, R. Mejía de Gutierrez, Evolution of binder structure in sodium silicate-activated slag-metakaolin blends, Cem. Concr. Compos. 33 (2011) 46–54, https://doi.org/10.1016/j.cemconcomp.2010.09.004.
[48] S. Zhang, Z. Li, B. Ghiassi, S. Yin, G. Ye, Fracture properties and microstructure formation of hardened alkali-activated slag/fly ash pastes, Cem. Concr. Res. 144 (2021), 106447, https://doi.org/10.1016/j.cemconres.2021.106447.
[49] N. Ye, J. Yang, X. Ke, J. Zhu, Y. Li, C. Xiang, H. Wang, L. Li, B. Xiao, Synthesis and characterization of Geopolymer from Bayer red mud with thermal pretreatment, J. Am. Ceram. Soc. 97 (2014) 1652–1660, https://doi.org/10.1111/jace.12840.
[50] M. Thiery, G. Villain, P. Dangla, G. Platret, Investigation of the carbonation front shape on cementitious materials: effects of the chemical kinetics, Cem. Concr. Res. 37 (2007) 1047–1058, https://doi.org/10.1016/j.cemconres.2007.04.002.
[51] A.F. Abdalqader, F. Jin, A. Al-Tabbaa, Characterisation of reactive magnesia and sodium carbonate-activated fly ash/slag paste blends, Constr. Build. Mater. 93 (2015) 506–513, https://doi.org/10.1016/j.conbuildmat.2015.06.015.
[52] A. Hajimohammadi, J.L. Provis, J.S.J. van Deventer, The effect of silica availability on the mechanism of geopolymerisation, Cem. Concr. Res. 41 (2011) 210–216, https://doi.org/10.1016/j.cemconres.2011.02.001.
[53] F. Reig, FTIR quantitative analysis of calcium carbonate (calcite) and silica (quartz) mixtures using the constant ratio method. Application to geological samples, Talanta 58 (2002) 811–821, https://doi.org/10.1016/S0039-9140(02)00372-7.
[54] A. Rađenović, J. Malina, T. Sofilić, Characterization of ladle furnace slag from carbon steel production as a potential adsorbent, Adv. Mater. Sci. Eng. 2013 (2013), e198240, https://doi.org/10.1155/2013/198240.
[55] J. Wang, Z. Hu, Y. Chen, J. Huang, Y. Ma, W. Zhu, J. Liu, Effect of Ca/Si and Al/Si on micromechanical properties of C(-A)-S-H, Cem. Concr. Res. 157 (2022), 106811, https://doi.org/10.1016/j.cemconres.2022.106811.
[56] E.N. Kani, H. Mehdizadeh, Investigating gel molecular structure and its relation with mechanical strength in geopolymer cement based on natural pozzolan using in situ ATR-FTIR spectroscopy, J. Mater. Civ. Eng. 29 (2017) 04017078, https://doi.org/10.1061/(ASCE)MT.1943-5533.0001917.
[57] I. García Lodeiro, D.E. Macphee, A. Palomo, A. Fernández-Jiménez, Effect of alkalis on fresh C-S–H gels. FTIR analysis, Cem. Concr. Res. 39 (2009) 147–153, https://doi.org/10.1016/j.cemconres.2009.01.003.
[58] S. Puligilla, P. Mondal, Co-existence of aluminosilicate and calcium silicate gel characterized through selective dissolution and FTIR spectral subtraction, Cem. Concr. Res. 70 (2015) 39–49, https://doi.org/10.1016/j.cemconres.2015.01.006.
[59] S. Choi, J.-M. Kim, D. Han, J.-H. Kim, Hydration properties of ladle furnace slag powder rapidly cooled by air, Constr. Build. Mater. 113 (2016) 682–690, https://doi.org/10.1016/j.conbuildmat.2016.03.089.
[60] B. Walkley, R. San Nicolas, M.-A. Sani, G.J. Rees, J.V. Hanna, J.S.J. van Deventer, J.L. Provis, Phase evolution of C-(N)-A-S-H/N-A-S-H gel blends investigated via alkali-activation of synthetic calcium aluminosilicate precursors, Cem. Concr. Res. 89 (2016) 120–135, https://doi.org/10.1016/j.cemconres.2016.08.010.
[61] I. Garcia-Lodeiro, A. Palomo, A. Fernández-Jiménez, D.E. Macphee, Compatibility studies between N-A-S-H and C-A-S-H gels. Study in the ternary diagram Na2O–CaO–Al2O3–SiO2–H2O, Cem. Concr. Res. 41 (2011) 923–931, https://doi.org/10.1016/j.cemconres.2011.05.006.
[62] A.M. Kaja, K. Schollbach, S. Melzer, S.R. van der Laan, H.J.H. Brouwers, Q. Yu, Hydration of potassium citrate-activated BOF slag, Cem. Concr. Res. 140 (2021), 106291, https://doi.org/10.1016/j.cemconres.2020.106291.
[63] Y. Ma, G. Ye, The shrinkage of alkali activated fly ash, Cem. Concr. Res. 68 (2015) 75–82, https://doi.org/10.1016/j.cemconres.2014.10.024.
[64] L. Li, W. Liu, Q. You, M. Chen, Q. Zeng, C. Zhou, M. Zhang, Relationships between microstructure and transport properties in mortar containing recycled ceramic powder, J. Clean. Prod. 263 (2020), 121384, https://doi.org/10.1016/j.jclepro.2020.121384.
[65] P. Duxson, J.L. Provis, G.C. Lukey, S.W. Mallicoat, W.M. Kriven, J.S.J. van Deventer, Understanding the relationship between geopolymer composition, microstructure and mechanical properties, Colloids Surf. A Physicochem. Eng. Asp. 269 (2005) 47–58, https://doi.org/10.1016/j.colsurfa.2005.06.060.
[66] L. Zheng, W. Wang, Y. Shi, The effects of alkaline dosage and Si/Al ratio on the immobilization of heavy metals in municipal solid waste incineration fly ash-based geopolymer, Chemosphere 79 (2010) 665–671, https://doi.org/10.1016/j.chemosphere.2010.02.018.
[67] B. Sun, G. Ye, G. de Schutter, A review: reaction mechanism and strength of slag and fly ash-based alkali-activated materials, Constr. Build. Mater. 326 (2022), 126843, https://doi.org/10.1016/j.conbuildmat.2022.126843.
[68] K.M. Klima, K. Schollbach, H.J.H. Brouwers, Q. Yu, Enhancing the thermal performance of class F fly ash-based geopolymer by sodalite, Constr. Build. Mater. 314 (2022), 125574, https://doi.org/10.1016/j.conbuildmat.2021.125574.
[69] K.M. Klima, K. Schollbach, H.J.H. Brouwers, Q. Yu, Thermal and fire resistance of class F fly ash based geopolymers – a review, Constr. Build. Mater. 323 (2022), 126529, https://doi.org/10.1016/j.conbuildmat.2022.126529.
[70] Z. Pan, J.G. Sanjayan, Factors influencing softening temperature and hot-strength of geopolymers, Cem. Concr. Compos. 34 (2012) 261–264, https://doi.org/10.1016/j.cemconcomp.2011.09.019.
[71] M. Lahoti, K.K. Wong, E.-H. Yang, K.H. Tan, Effects of Si/Al molar ratio on strength endurance and volume stability of metakaolin geopolymers subject to elevated temperature, Ceram. Int. 44 (2018) 5726–5734, https://doi.org/10.1016/j.ceramint.2017.12.226.
[72] D. Yan, Y. Zhang, S. Chen, H. Fazli, Y. Liu, Y. Ao, Effect of silica moduli on the thermal degradation mechanisms of Fly ash-based geopolymer mortars, J. Mater. Civ. Eng. 33 (2021) 04021059, https://doi.org/10.1061/(ASCE)MT.1943-5533.0003669.
[73] A. Natali Murri, W.D.A. Rickard, M.C. Bignozzi, A. van Riessen, High temperature behaviour of ambient cured alkali-activated materials based on ladle slag, Cem. Concr. Res. 43 (2013) 51–61, https://doi.org/10.1016/j.cemconres.2012.09.011.
[74] Z. Pan, J.G. Sanjayan, B.V. Rangan, An investigation of the mechanisms for strength gain or loss of geopolymer mortar after exposure to elevated temperature, J. Mater. Sci. 44 (2009) 1873–1880, https://doi.org/10.1007/s10853-009-3243-z.
[75] X. Liu, P. Feng, C. Lyu, S. Ye, The role of sulfate ions in tricalcium aluminate hydration: new insights, Cem. Concr. Res. 130 (2020), 105973, https://doi.org/10.1016/j.cemconres.2020.105973.
[76] J. Havlica, D. Roztocká, S. Sahu, Hydration kinetics of calciumaluminate phases in the presence of various ratios of Ca2+ and ions in liquid phase, Cem. Concr. Res. 23 (1993) 294–300, https://doi.org/10.1016/0008-8846(93)90094-P.

[77] J. Ding, Y. Fu, J.J. Beaudoin, Strätlingite formation in high-alumina cement — zeolite systems, Adv. Cem. Res. 7 (1995) 171–178, https://doi.org/10.1680/adcr.1995.7.28.171.
[78] G. Le Saoût, B. Lothenbach, A. Hori, T. Higuchi, F. Winnefeld, Hydration of Portland cement with additions of calcium sulfoaluminates, Cem. Concr. Res. 43 (2013) 81–94, https://doi.org/10.1016/j.cemconres.2012.10.011.
[79] A. Rafeet, R. Vinai, M. Soutsos, W. Sha, Effects of slag substitution on physical and mechanical properties of fly ash-based alkali activated binders (AABs), Cem. Concr. Res. 122 (2019) 118–135, https://doi.org/10.1016/j.cemconres.2019.05.003.
[80] A.M. Kaja, A. Lazaro, Q.L. Yu, Effects of Portland cement on activation mechanism of class F fly ash geopolymer cured under ambient conditions, Constr. Build. Mater. 189 (2018) 1113–1123, https://doi.org/10.1016/j.conbuildmat.2018.09.065.